



## Advantages of high quality SWIR bands for ocean colour processing: Examples from Landsat-8



Quinten Vanhellemont<sup>\*</sup>, Kevin Ruddick

Royal Belgian Institute of Natural Sciences (RBINS), Operational Directorate Natural Environment, 100 Gulledele, 1200 Brussels, Belgium

### ARTICLE INFO

#### Article history:

Received 21 October 2014

Received in revised form 27 January 2015

Accepted 4 February 2015

Available online 4 March 2015

#### Keywords:

Landsat-8

Turbid waters

SWIR

Atmospheric correction

Suspended particulate matter

Sediment type

### ABSTRACT

Monitoring of water quality by satellite ocean colour data requires high quality atmospheric correction and especially the accurate quantification of the aerosol contribution to the top of atmosphere radiance. Several methods have been proposed for atmospheric correction over turbid waters, including modelling the marine contributions to the NIR signal or switching to longer short-wave infrared (SWIR) wavelengths where the signal even in turbid waters can be assumed zero. Here we present the use of the high quality SWIR bands of the Operational Land Imager (OLI) on Landsat-8, launched in 2013, to extend our existing turbid water atmospheric correction to extremely turbid waters. The atmospheric correction is image based, and no external measurements are required. The aerosol type is estimated using NIR and SWIR bands in clear water pixels, or in all water pixels using the two SWIR bands. The aerosol type is assumed to be constant over a single Landsat-8 tile (170 by 185 km), or allowed to vary spatially when using both SWIR bands. Realistic spatial patterns of marine reflectances are retrieved, uncorrelated with the estimated aerosol reflectance. Taking spatial and temporal variability into account, products from Landsat-8 compare well with those of MODIS Aqua and Terra — also using the SWIR bands for atmospheric correction. The limitations of our previously published method (Vanhellemont & Ruddick, 2014a) are illustrated at higher turbidities, and removed by using the new method. The uncertainty caused by using a single aerosol type per scene is assessed. The advantages of the high spatial resolution L8/OLI data are clear for applications in coastal and estuarine waters. As an example of the advantage of high quality SWIR bands, and a SWIR-based atmospheric correction, an algorithm for detecting black suspended sediments from dredging and dumping operations is demonstrated here. In conclusion, L8/OLI is a powerful new tool for remote sensing of extremely turbid waters, and can be used as a precursor for future ocean colour missions with SWIR bands.

© 2015 The Authors. Published by Elsevier Inc. This is an open access article under the CC BY-NC-ND license (<http://creativecommons.org/licenses/by-nc-nd/4.0/>).

### 1. Introduction

The European Union Marine Strategy Framework Directive (MSFD, 2008/56/EC) and Water Framework Directive (WFD, 2000/60/EC and amendments) require the member states to monitor the state of the marine environment. The WFD includes inland waters and marine waters up to the first nautical mile from the coast, and the MSFD obliges members to achieve and maintain a Good Environmental Status (GES) of all marine waters by 2020. Remote sensing is a cost effective way to accomplish monitoring of turbidity and chlorophyll *a* concentration at a large and transboundary scale. However, due to riverine sediment inputs or due to resuspension of bottom sediments, coastal waters are often quite turbid, which poses problems for typical atmospheric correction methods. Moreover, the WFD focuses on the first nautical mile from the coast, and ocean colour satellites have a quite coarse “moderate” resolution (250 to 1000 m pixel size), and due to a number of problems (mixed land–sea pixels, adjacency, stray light) their data is

practically unusable in this first nautical mile. Imagery from higher resolution sensors, such as Landsat-8 and the upcoming Sentinel-2, with an appropriate turbid water atmospheric correction, is thus of great interest to coastal and inland water quality monitoring in general (Vanhellemont & Ruddick, 2014a,b), and specifically for the WFD. For extremely turbid waters, assumptions made by Vanhellemont and Ruddick (2014a) are invalid, and their method will need to be revised.

Atmospheric correction of satellite imagery over turbid waters requires separation of aerosol and marine contributions from the top of atmosphere signal observed by the satellite. The open ocean atmospheric correction schemes typically use two or more NIR bands where the marine signal is assumed to be zero (Gordon & Wang, 1994). For clear waters this is a valid assumption, as the pure water absorption is very high in the NIR, and there is little or no contribution from suspended particles. The signal in the NIR bands can thus be assumed to be entirely atmospheric, and is used to determine an aerosol model. With this aerosol model, the aerosol reflectance is extrapolated to the visible bands. In turbid waters however, due to high concentrations of particulate matter the signal in the NIR is not negligible. In many cases the brightness of turbid waters even triggers threshold based cloud masking schemes (Nordkvist, Loisel,

<sup>\*</sup> Corresponding author.

E-mail address: [quinten.vanhellemont@naturalsciences.be](mailto:quinten.vanhellemont@naturalsciences.be) (Q. Vanhellemont).

& Gaurier, 2009; Wang & Shi, 2006). If the marine contribution of turbid waters is not properly taken into account, the aerosol reflectance is overestimated, leading to low and even negative marine reflectances in the visible bands (Ruddick, Ovidio, & Rijkeboer, 2000). To extend the (Gordon & Wang, 1994) atmospheric correction to turbid waters, common approaches are to (1) model the marine contributions to the NIR bands (Hu, Carder, & Muller-Karger, 2000; Moore, Aiken, & Lavender, 1999; Ruddick et al., 2000; Stumpf, Arnone, Gould, Martinolich, & Ransibrahmanakul, 2003), or (2) use short-wave infrared (SWIR) wavelengths (Wang & Shi, 2005). The latter approach can be applied to the 1609 and 2201 nm bands of Landsat-8, where even in turbid waters the marine signal can be assumed zero. The first approach is essential for sensors without SWIR bands, such as the Sea-viewing Wide Field-of-view Sensor (SeaWiFS), the Medium Resolution Imaging Spectroradiometer (MERIS) and the Geostationary Ocean Color Imager (GOCI). For observing highly turbid waters within the GOCI field of view, a model has been developed (Wang, Shi, & Jiang, 2012), but as of now no generic method exists. Not many ocean colour sensors have SWIR bands, and existing SWIR bands often have significant noise levels.

An iterative scheme for modelling non-zero NIR reflectances of highly productive waters was adopted in the SeaDAS processing (Bailey, Franz, & Werdell, 2010; Stumpf et al., 2003) and performs reasonably well in low to moderately turbid waters (Goyens, Jamet, & Schroeder, 2013; Vanhellemont, Greenwood, & Ruddick, 2013). For turbid waters dominated by suspended sediments, the NIR signal can be modelled using a constant marine reflectance ratio in two NIR bands and the assumption of a constant aerosol type over the (sub)scene, that is derived from clear water pixels where the NIR reflectance is effectively zero (Ruddick et al., 2000). However, at very high turbidities the relationship between the marine signal in the NIR bands is not linear (Doron, Bélanger, Doxaran, & Babin, 2011; Shi & Wang, 2009) and more accurate modelling of the spectral relationship between the NIR bands is required (Goyens, Jamet, & Ruddick, 2013; Wang et al., 2012). A similar approach was used for sensors with a red and NIR band (Neukermans et al., 2009; Vanhellemont & Ruddick, 2014a), for which the assumption of a linear relationship in the two bands is invalid even at moderate turbidities (suspended particulate matter concentration exceeding  $\sim 30 \text{ g m}^{-3}$ ). Recently, a technique merging the advantages of these methods provided good results for turbid waters (Jiang & Wang, 2014), but the authors still recommended directly deriving the NIR marine signal using a SWIR-based atmospheric correction.

In the shortwave infrared (SWIR) part of the spectrum ( $1 \mu\text{m} < \lambda < 3 \mu\text{m}$ ), the pure-water absorption is very high (Kou, Labrie, & Chylek, 1993), and at longer SWIR wavelengths ( $\lambda > 1.6 \mu\text{m}$ ), even extremely turbid waters are effectively black (Shi & Wang, 2009). Non-zero marine reflectances have only been observed at shorter SWIR wavelengths, 1020 and 1240 nm (Knaeps, Dogliotti, Raymaekers, Ruddick, & Sterckx, 2012; Shi & Wang, 2009, 2014). There is currently no dedicated ocean colour SWIR band on any satellite-borne sensor, but the SWIR bands on MODIS have shown potential for a SWIR based atmospheric correction method over highly turbid waters (Wang & Shi, 2007). The products derived from the MODIS SWIR correction are quite noisy, due to the

low signal-to-noise ratio (SNR) of the bands, and this is considered the main drawback of the method (Wang & Shi, 2012; Werdell, Franz, & Bailey, 2010). Typically, for SWIR correction of MODIS Aqua data, the 1240 nm and 2130 nm bands are used, as the 1640 nm band has a number of broken detectors. Similar SWIR bands are present on the Visible Infrared Imaging Radiometer Suite (VIIRS), and VIIRS data was processed for extremely turbid waters using bands at 1238 and 1610 nm, because the band at 2250 nm has remaining calibration issues (Jiang & Wang, 2014).

The Operational Land Imager (OLI) on board of Landsat-8 (L8/OLI) has been demonstrated to be a useful tool for monitoring of coastal sediments at high resolution and at high quality due to the higher SNR compared to previous Landsat imagers (Vanhellemont & Ruddick, 2014a). For the atmospheric correction, Vanhellemont and Ruddick (2014a) assumed a linear relationship between the water-leaving radiance reflectances in the red (band 4, 655 nm) and NIR (band 5, 865 nm) bands on OLI ( $\alpha = \rho_w^4 / \rho_w^5 = 8.7$ ) and a per-tile fixed aerosol type ( $\epsilon$ ). In highly turbid waters this method will overestimate aerosol reflectance due to the non-linearity of the  $\rho_w^4 / \rho_w^5$  ratio. The aerosol type can vary spatially in nature, and for scenes with a large distance between turbid and clear waters a single  $\epsilon$  may not be appropriate (Jiang & Wang, 2014). Moreover, in scenes without clear water pixels – due to cloud cover or the limited footprint of a Landsat tile, estimation of the aerosol type using the red and NIR band pair will be impossible as it relies on pixels where the water can be assumed black in the NIR.

Here we present an automatic method for atmospheric correction over extremely turbid waters using the SWIR bands of L8/OLI. The SWIR bands are used both for water pixel detection and aerosol correction. Our previously published method (Vanhellemont & Ruddick, 2014a) is thus extended to extremely turbid waters, and its validity range is examined using the new algorithm. As with the previous method, no in situ measurements are required and the method can be applied immediately to any L8/OLI tile. Apart from a negligible reflectance in the 1609 and 2201 nm SWIR bands ( $\rho_w^6 = \rho_w^7 = 0$ ), no assumptions have to be made on the marine reflectances. An assessment is made of assumptions on the spatial distribution of aerosol types and the impact on marine products.

## 2. Methods

The Operational Land Imager on Landsat-8 (L8/OLI) is a 9 band push-broom imager with 8 channels at 30 m spatial resolution and one panchromatic channel at 15 m spatial resolution (Table 1). The SWIR bands in Table 1 is specified for terrestrial reference radiances, which are appropriate for top-of-atmosphere typical open ocean radiances in the visible and NIR, but are about a factor 10 higher in the SWIR (Hu et al., 2012). L8 follows the Worldwide Reference System 2 orbit and has a track repeat cycle of 16 days, but at higher latitudes overlap between tracks is possible. L8/OLI imagery (images listed in Table 2) at L1T was obtained free of charge from EarthExplorer (<http://earthexplorer.usgs.gov/>) and top-of-atmosphere (TOA) radiances,  $L_{\text{TOA}}$ , were computed from digital numbers, DN:

$$L_{\text{TOA}} = M_L \cdot \text{DN} + A_L \quad (1)$$

**Table 1**  
L8/OLI bands with wavelength, ground sampling distance, GSD, signal-to-noise ratio, SNR; at reference radiance, L, (Irons, Dwyer, & Barsi, 2012) and band average extraterrestrial solar irradiance, F0. Band averaged wavelengths are given in square brackets.

Band	Wavelength (nm) range	[Central]	GSD (m)	SNR at reference L	Reference L ( $\text{W m}^{-2} \text{sr}^{-1} \mu\text{m}^{-1}$ )	F0 ( $\text{W m}^{-2} \mu\text{m}^{-1}$ )
1 (Coastal/aerosol)	433–453	[443]	30	232	40	1895.6
2 (Blue)	450–515	[483]	30	355	40	2004.6
3 (Green)	525–600	[561]	30	296	30	1820.7
4 (Red)	630–680	[655]	30	222	22	1549.4
5 (NIR)	845–885	[865]	30	199	14	951.2
6 (SWIR 1)	1560–1660	[1609]	30	261	4	247.6
7 (SWIR 2)	2100–2300	[2201]	30	326	1.7	85.5
8 (PAN)	500–680	[591]	15	146	23	1724.0
9 (CIRRUS)	1360–1390	[1373]	30	162	6	367.0

**Table 2**

L8/OLI images used in this paper, with image identifier, WRS-2 path and row, date and time (ISO8601). All L1T images were processed with LGPS 2.3.0. Images in *italic* are only shown in Supplementary data 2.

Image	WRS-2 TILE PATH-ROW	Date/time (ISO8601)
LC81990242013248LGN00	P199-R024	2013-09-05T10:42Z
LC81990242013280LGN00	P199-R024	2013-10-07T10:41Z
LC82000242013303LGN00	P200-R024	2013-10-30T10:47Z
<i>LC81990242013344LGN00</i>	<i>P199-R024</i>	<i>2013-12-10T10:41Z</i>
<i>LC82000242014034LGN00</i>	<i>P200-R024</i>	<i>2014-02-03T10:47Z</i>
LC81990242014075LGN00	P199-R024	2014-03-18T10:40Z
<i>LC81990242014091LGN00</i>	<i>P199-R024</i>	<i>2014-04-01T10:40Z</i>

with  $M_L$  (multiplicative factor, gain) and  $A_L$  (additive factor, offset) values provided in the Level 1 Product Generation System (LPGS version 2.3.0) metadata file. TOA reflectances ( $\rho_{TOA}$ ) were computed by normalizing  $L_{TOA}$  to the band averaged irradiance:

$$\rho_{TOA} = \frac{\pi \cdot L_{TOA} \cdot d^2}{FO \cdot \cos\theta_0} \quad (2)$$

where  $FO$  is the band averaged extraterrestrial solar irradiance,  $d$  the sun-earth distance in Astronomical Units, and  $\theta_0$  the sun zenith angle.  $\rho_{TOA}$  is assumed to be the sum of aerosol reflectance ( $\rho_a$ ), Rayleigh reflectance ( $\rho_r$ ) and the water-leaving radiance reflectance just above the surface ( $\rho_w^{0+}$ ):

$$\rho_{TOA} = \rho_a + \rho_r + t \cdot \rho_w^{0+} \quad (3)$$

with  $t$  the two-way diffuse atmospheric transmittance.  $\rho_w^{0+}$  is defined as:

$$\rho_w^{0+} = \frac{\pi \cdot L_w^{0+}}{E_d^{0+}}, \quad (4)$$

where  $L_w^{0+}$  is the water-leaving radiance, and  $E_d^{0+}$  the down-welling irradiance, both just above the water surface. Hereafter the superscript is dropped from  $\rho_w^{0+}$ , and  $\rho_w$  will for brevity also be referred to as marine reflectance. The Rayleigh correction of Vanhellemont and Ruddick (2014a, b) is updated to a look-up-table (LUT) generated for all OLI bands (square bandpass) using 6SV v1.1 (Vermette et al., 2006), modified to disable the ocean contribution but including sea surface reflectance (sky- and sunglint) for a nominal wind speed of  $1 \text{ m s}^{-1}$ . The Rayleigh reflectance is then easily obtained from the LUT using sun and sensor geometry. Cloud and land masking is performed using a threshold on the reflectance in the 1609 nm SWIR band, as suggested by Wang and Shi (2006). Pixels are classified as not being water when the Rayleigh-corrected reflectance ( $\rho_c = \rho_{TOA} - \rho_r$ ) in band 6,

$$\rho_c^6 > 0.0215. \quad (5)$$

This simple threshold method works well throughout the world for discriminating water from floating objects, offshore constructions, land and clouds, even in extremely turbid waters. It has some difficulties with cloud and mountain shadows, as both can be quite dark in the SWIR. In cases where cloud shadows over land and mountain shadows are misclassified as water, additional masking could be performed using an external land mask, but then extra care is required for intertidal areas. The threshold can be defined on an image by image basis, and might need to be adapted for different regions. Areas with high sun glint are also masked using the threshold method.

Different aerosol corrections are compared in this paper (overview in Table 3), using different band pairs for the aerosol type selection. Aerosol type ( $\varepsilon$ ) is determined from the ratio of reflectances in the band pair, over water pixels where the marine contribution in those bands can be assumed to be zero. The  $\varepsilon$  is then used to extrapolate the observed aerosol reflectance to the visible channels. One method uses the red and NIR bands (Vanhellemont & Ruddick, 2014a), hereafter VR-NIR. Three new methods use different band pairs: two NIR-SWIR pairs, using bands 5 and 6, and bands 5 and 7 and one using both SWIR bands, 6 and 7, hereafter VR-SWIR. If needed for clarification, bands used for the aerosol selection will be given between brackets (S, L), with the shortest (S) and longest (L) waveband used. The band numbers can also be specified with the aerosol type (e.g.,  $\varepsilon^{S,L}$ ). The VR-SWIR (6,7) method was also applied with a per scene fixed ( $-F$ ) and per pixel variable ( $-V$ ) aerosol type, as all water pixels can be assumed to be black at both SWIR wavelengths (1609 and 2201 nm). Other variations on variable and fixed aerosol type and concentration are discussed further in Supplementary data 1.

In VR-NIR (4,5), the aerosol reflectance is estimated by assuming a linear relationship between marine reflectances in bands 4 and 5 ( $\alpha = \rho_w^4 / \rho_w^5 = 8.7$ ), and constant aerosol type ( $\varepsilon$ ) over the scene.  $\varepsilon$  can be derived from the slope of the regression line (see Fig. 6 of Neukermans et al., 2009) or the median ratio of Rayleigh corrected reflectances in bands 4 and 5 ( $\rho_c^4, \rho_c^5$ ) over clear water pixels. In this paper the median ratio will be used as it is less sensitive to outliers than a regression analysis. Clear water pixels are automatically determined after first processing the scene with  $\varepsilon = 1$  and then selecting pixels where the resulting  $\rho_w^4 < 0.005$ .

In VR-SWIR, the atmospheric correction scheme is simpler than VR-NIR, as at least one of the bands used (in the SWIR) has a negligible marine signal. One of the advantages of using the two SWIR bands (6,7) is that clear water pixels do not have to be selected before aerosol type selection, as both bands are assumed to have a zero marine contribution. Additionally, a per-pixel variable  $\varepsilon$  can be calculated for a comparison with the processing that assumes a spatially invariant aerosol type. For the combinations using the NIR band (5), the reasoning is as follows:

$$\rho_c^5 = \rho_{am}^5 + t^5 \rho_w^5 \quad (6)$$

**Table 3**

Different atmospheric correction methods used for L8/OLI.

Method	Bands used for aerosol correction	$\varepsilon$ spatial assumption	Aerosol $\varepsilon$ determination	Reference
VR-NIR (4,5)	655, 865 nm	Fixed	Median, clear waters ( $\rho_w^4 < 0.005$ ) Iteratively, first $\varepsilon = 1$	Vanhellemont and Ruddick (2014a)
VR-SWIR (5,6)	865, 1609 nm	Fixed	Median, clear waters (Spectral test on $\rho_c$ )	This paper
VR-SWIR (5,7)	865, 2201 nm	Fixed	Median, clear waters (Spectral test on $\rho_c$ )	This paper
VR-SWIR (6,7)-F	1609, 2201 nm	Fixed	Median, all water pixels (Spectral test on $\rho_c$ )	This paper
VR-SWIR (6,7)-V	1609, 2201 nm	Variable	Per pixel	This paper
SD-SWIR	1609, 2201 nm	Variable	Per pixel	SeaDAS: <a href="http://seadas.gsfc.nasa.gov/">http://seadas.gsfc.nasa.gov/</a> (Franz et al., 2014)
SD-MUMM	1609, 2201 nm	Fixed	Median derived from VR-SWIR (6,7)	SeaDAS: <a href="http://seadas.gsfc.nasa.gov/">http://seadas.gsfc.nasa.gov/</a> (Franz et al., 2014)

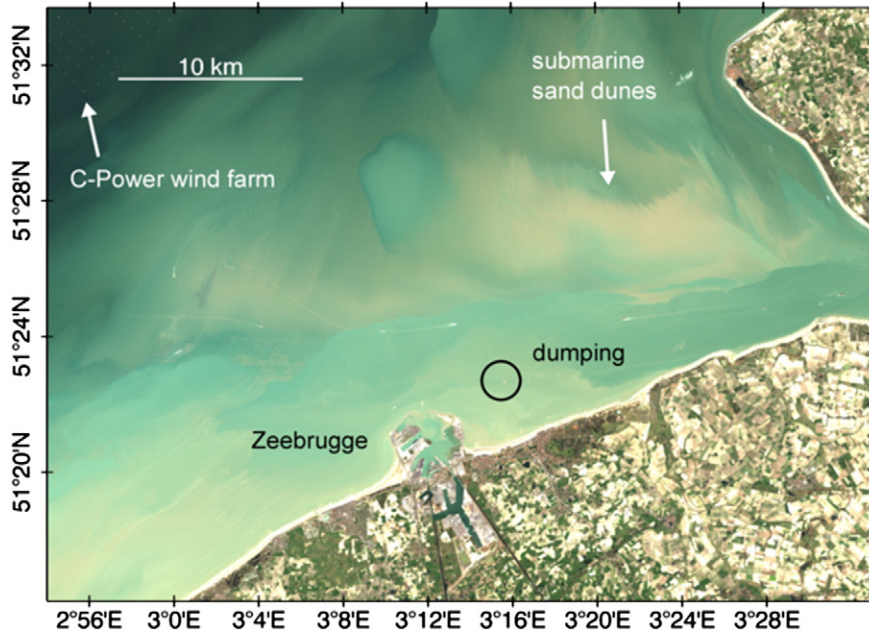


**Fig. 1.** Rayleigh corrected RGB (channels 4–3–2) OLI image over Belgian coastal waters (2014-03-16, scene LC81990242014075LGN00), showing turbid coastal waters with high sediment concentration (yellow-brown). The circle shows dumping of dredged material at a designated site (other example in Fig. 13 and (Vanhellemont & Ruddick, 2014b), see zoomed version in Fig. 2).

$$\rho_c^L = \rho_{am}^L \quad (\rho_w^L = 0) \quad (7)$$

where  $\rho_c^i$  is the Rayleigh corrected reflectance,  $\rho_{am}^i$  the multiple scattering aerosol reflectance,  $t^i$  the atmospheric transmittance, and  $\rho_w^i$  the marine reflectance in band  $i$ . The  $L$  superscript refers to the SWIR band used in the correction, band 6 or 7. The aerosol type,  $\epsilon^{5,L}$ , is considered constant

over the scene and can be determined from clear water pixels as the slope of the regression line  $\rho_c^L$  vs  $\rho_c^5$  or the median of the  $\rho_c^L : \rho_c^5$  ratio. Here we again use the median, as it allows for a more robust determination, relatively insensitive to outliers. Clear water pixels were selected by constraining the data to pixels where:

$$\frac{\rho_c^L + 0.005}{\rho_c^5} > 0.8. \quad (8)$$

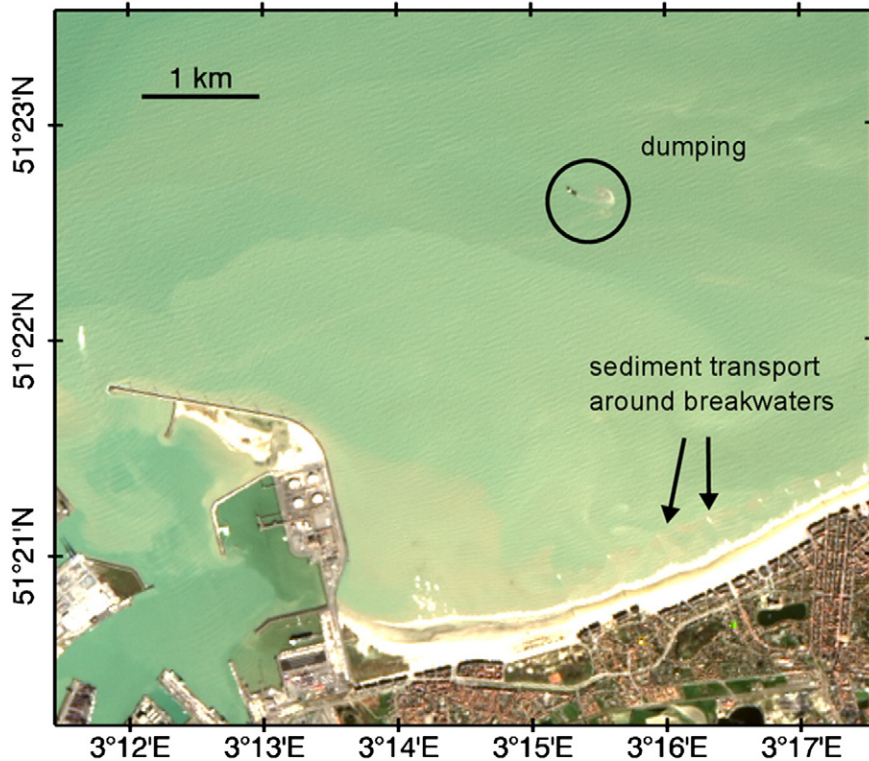


**Fig. 2.** Crop of Fig. 1 showing the dumping of dredged material at a designated site. Surface gravity waves can be seen at this resolution.

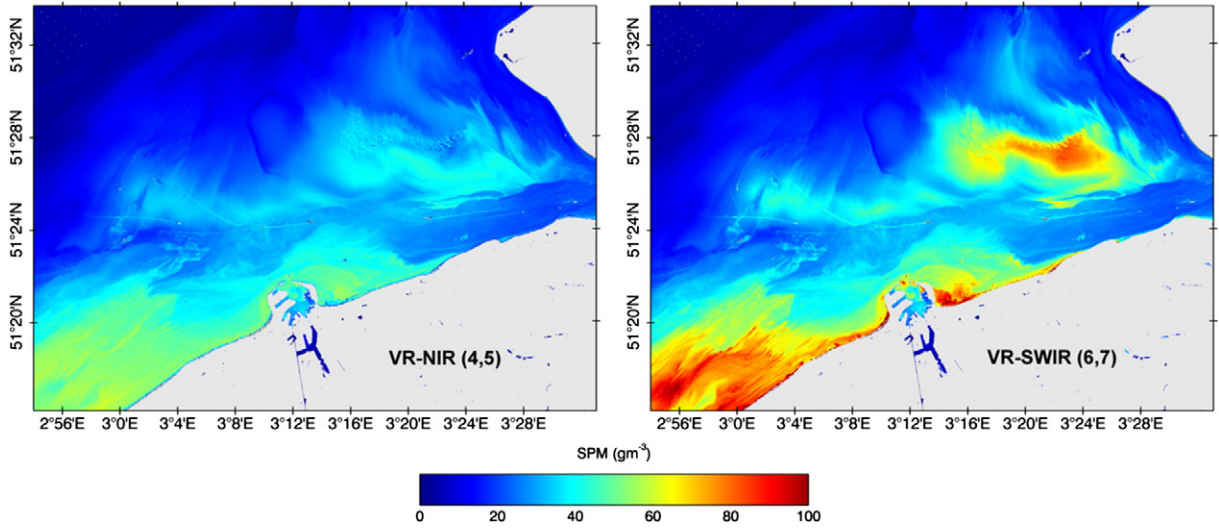


Fig. 3. OLI-derived suspended particulate matter concentration (SPM) over Belgian coastal waters (2014-03-16, scene LC81990242014075LGN00) processed using the VR-NIR 4,5 (left) and VR-SWIR 6,7 (right) methods.

Eq. (8) excludes turbid waters by removing pixels where the NIR reflectance is higher than what is expected from the aerosol reflectance in band L. The offset of 0.005 is included to retain low reflectance pixels where the ratio threshold is too restrictive.  $\rho_w^5$  can then be computed using:

$$\rho_w^5 = \frac{1}{t^5} (\rho_c^5 - \varepsilon^{5,L} \rho_{am}^L). \quad (9)$$

In the case of using the two SWIR bands,  $\varepsilon^{6,7}$  is easily calculated from  $\rho_c^6$  and  $\rho_c^7$ , which are assumed to have zero marine contributions. A pixel-by-pixel  $\varepsilon^{6,7}$  can be computed, or a single value per scene can be estimated from  $\rho_c^7$ ,  $\rho_c^6$ , using the median ratio or regression slope. The former allows for spatially varying aerosols, the latter minimizes impact of noise in the SWIR bands.

Spectral  $\varepsilon$  is derived using the simple exponential extrapolation (Gordon & Wang, 1994):

$$\varepsilon^{i,L} = (\varepsilon^{S,L})^{\delta i} \quad (10)$$

where L and S are the longest (5, 6 or 7) and shortest (4, 5 or 6) wavelength bands used, and

$$\delta i = \frac{\lambda_L - \lambda_i}{\lambda_L - \lambda_S} \quad (11)$$

$\rho_w$  at other wavelengths can then be derived from  $\rho_c$ :

$$\rho_w^i = \frac{1}{t^i} (\rho_c^i - \varepsilon^{i,L} \rho_{am}^L). \quad (12)$$

At present insufficient in situ data are available for the validation of OLI products, although a preliminary validation using Aeronet-OC data (Zibordi et al., 2009) was performed by (Vanhellemont, Bailey, Franz, & Shea, 2014), showing good agreement between OLI and in situ spectra. In this study, imagery from the well-established Moderate Resolution Spectroradiometers (MODIS) on the Aqua and Terra platforms are used for the validation. The closest available (same day) L1A scenes were selected and processed to L2 using SeaDAS version 7.0.2. Images were processed at 250 m resolution using the Gordon and Wang

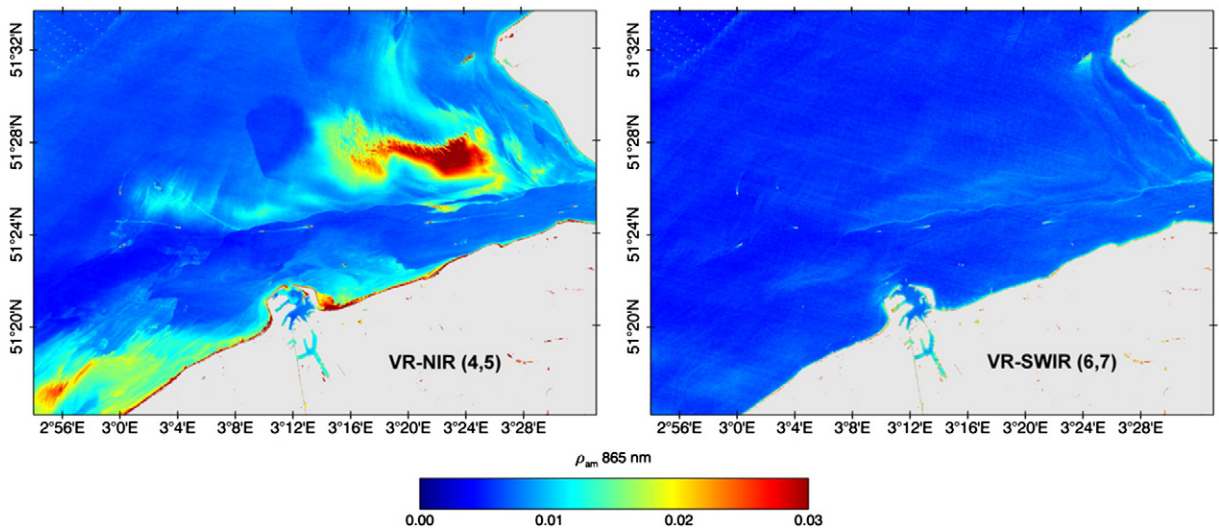
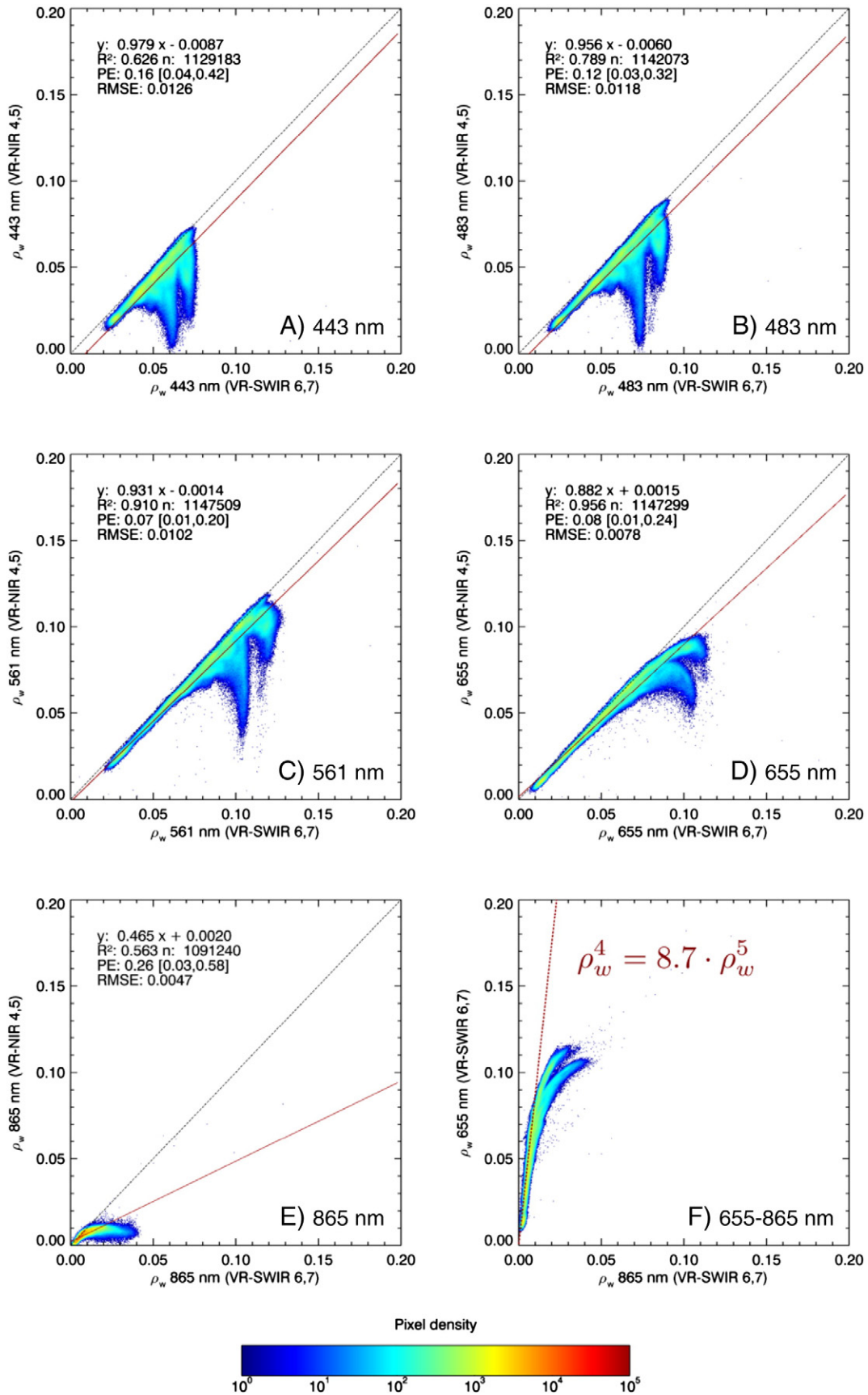
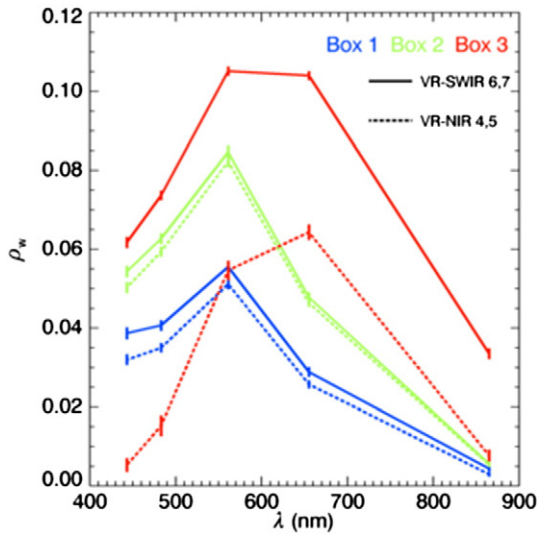


Fig. 4. Multiple scattering aerosol reflectance at 865 nm ( $\rho_{am}^{865nm}$ ) from the 2014-03-16 image over Belgian coastal waters (2014-03-16, scene LC81990242014075LGN00) processed using the VR-NIR 4,5 (left) and VR-SWIR 6,7 (right) methods.



**Fig. 5.** Scatter plots showing (A) through (E) the comparison of water-leaving radiance reflectances ( $\rho_w$ ), at 443, 483, 561, 655 and 865 nm, derived from the 2014-03-16 image over Belgian coastal waters (2014-03-16, scene LC81990242014075LGN00) using the VR-NIR 4,5 (y) and VR-SWIR 6,7 (x) processing methods. Colours denote pixel densities, the dashed black line is the 1:1 line, and the Reduced Major Axis (RMA) regression line is drawn in red. (F) Comparison between  $\rho_w^5$  and  $\rho_w^4$  derived from the VR-SWIR 6,7 processing, the dashed red line shows the assumption made on marine reflectances in VR-NIR 4,5 ( $\rho_w^4 = 8.7 \cdot \rho_w^5$ ). For all scatter plots, points are included after a 10 pixel (300 m) dilation of masked (land/cloud) pixels.



**Fig. 6.** Median water-leaving radiance reflectance ( $\rho_w$ ) from three 60 by 60 pixel boxes extracted from the 2014-03-16 image, ranging from relatively clear (box 1) to extremely turbid waters (box 3), processed using VR-SWIR 6,7 (solid lines) and VR-NIR 4,5 (dashed lines). The VR-NIR atmospheric correction fails in Box 3, due to the wrong estimation of aerosol reflectance. The location of the boxes is shown in Fig. 7. Vertical lines show the RMSD within the box.

(1994) approach but using the SWIR bands (1240 and 2130 nm) for aerosol selection, as suggested by Wang (2007). The aerosol reflectance is then extrapolated from the SWIR to the visible channels using the two best fitting out of eighty aerosol models per pixel. The standard chlorophyll based BRDF correction (Morel & Gentili, 1996) and land masking were disabled. Cloud screening was performed using a threshold ( $>0.018$ ) on surface reflectance in the 2201 nm band. MODIS imagery was then resampled to the corresponding Landsat tile, averaging overlapping scans where necessary.

For evaluation of our simple processing method, the OLI images are also processed using the upcoming SeaDAS implementation (Franz, Bailey, Kuring, & Werdell, 2014; Vanhellemont, Bailey et al., 2014), according to (Gordon & Wang, 1994) using the SWIR bands (6 and 7) for aerosol model selection (hereafter SD-SWIR). The MUMM approach (Ruddick et al., 2000) was also applied (hereafter SD-MUMM), using the SWIR bands and an aerosol  $\epsilon$  derived from our VR-SWIR (6,7) processing (see above). For both methods, cloud masking was done using a threshold of 0.0215 on surface reflectance in the 1609 nm channel. Similar to the MODIS processing, the standard land masking and the BRDF correction were disabled. While our new method is very fast and easily understood, SeaDAS has a more complete treatment of aerosol transmittances, multiple scattering and uses relatively high frequency ancillary gas and pressure data – albeit at a low spatial resolution for L8/OLI. In SeaDAS, the aerosol epsilon is extrapolated using an aerosol model rather than using an exponential extrapolation. Additionally, SeaDAS is easily available and a well-supported platform.

**Table 4**

Comparison of different atmospheric correction methods (Table 3) over three 60 × 60 boxes of apparent homogeneous water pixels (see Fig. 7) from the 2014-03-16 OLI image over the Belgian coastal zone. Median values of  $\rho_w$  and RMSD are given and the RMSD relative to the  $\rho_w$ . VR-NIR fails in box 3 (Fig. 3) by overestimating  $\rho_{am}$  and underestimating  $\rho_w$  (bad retrievals are underlined).

Band	Method	Box 1			Box 2			Box 3		
		$\rho_w$ (P50)	RMSD (P50)	%	$\rho_w$ (P50)	RMSD (P50)	%	$\rho_w$ (P50)	RMSD (P50)	%
443 nm	VR-NIR (4,5)	0.0319	0.0014	4.4	0.0503	0.0014	2.9	0.0053	0.0018	<u>33.4</u>
	VR-SWIR (5,6)	0.0309	0.0018	5.9	0.0462	0.0017	3.8	0.0515	0.0017	3.3
	VR-SWIR (5,7)	0.0334	0.0021	6.4	0.0487	0.0020	4.2	0.0545	0.0020	3.7
	VR-SWIR (6,7)	0.0386	0.0015	4.0	0.0543	0.0015	2.8	0.0617	0.0014	2.3
	VR-SWIR (6,7) ve	0.0357	0.0042	11.7	0.0513	0.0042	8.1	0.0588	0.0042	7.1
	SD-SWIR	0.0268	0.0057	21.1	0.0428	0.0055	12.9	0.0493	0.0055	11.3
	SD-MUMM	0.0330	0.0021	6.4	0.0488	0.0020	4.0	0.0553	0.0020	3.6
	483 nm	VR-NIR (4,5)	0.0350	0.0012	3.5	0.0593	0.0013	2.2	0.0152	0.0027
VR-SWIR (5,6)		0.0339	0.0016	4.7	0.0555	0.0016	2.8	0.0648	0.0014	2.2
VR-SWIR (5,7)		0.0360	0.0019	5.2	0.0577	0.0019	3.3	0.0673	0.0017	2.6
VR-SWIR (6,7)		0.0406	0.0014	3.3	0.0626	0.0014	2.2	0.0736	0.0012	1.6
VR-SWIR (6,7) ve		0.0380	0.0036	9.6	0.0599	0.0037	6.1	0.0711	0.0036	5.0
SD-SWIR		0.0319	0.0050	15.8	0.0549	0.0048	8.7	0.0657	0.0047	7.2
SD-MUMM		0.0375	0.0018	4.8	0.0602	0.0017	2.8	0.0708	0.0016	2.3
561 nm		VR-NIR (4,5)	0.0511	0.0014	2.7	0.0822	0.0015	1.9	0.0546	0.0025
	VR-SWIR (5,6)	0.0499	0.0017	3.5	0.0787	0.0018	2.3	0.0978	0.0013	1.4
	VR-SWIR (5,7)	0.0515	0.0020	3.8	0.0804	0.0020	2.5	0.0997	0.0016	1.6
	VR-SWIR (6,7)	0.0555	0.0016	2.8	0.0846	0.0017	2.0	0.1051	0.0012	1.1
	VR-SWIR (6,7) ve	0.0532	0.0032	6.0	0.0822	0.0033	4.0	0.1029	0.0031	3.0
	SD-SWIR	0.0573	0.0039	6.8	0.0894	0.0036	4.0	0.1125	0.0032	2.9
	SD-MUMM	0.0616	0.0016	2.6	0.0932	0.0016	1.7	0.1159	0.0013	1.1
	655 nm	VR-NIR (4,5)	0.0257	0.0011	4.2	0.0464	0.0011	2.3	0.0643	0.0020
VR-SWIR (5,6)		0.0245	0.0013	5.4	0.0433	0.0013	2.9	0.0983	0.0013	1.3
VR-SWIR (5,7)		0.0257	0.0016	6.1	0.0445	0.0015	3.5	0.0996	0.0015	1.5
VR-SWIR (6,7)		0.0288	0.0013	4.4	0.0478	0.0012	2.6	0.1039	0.0012	1.1
VR-SWIR (6,7) ve		0.0270	0.0025	9.2	0.0459	0.0025	5.4	0.1019	0.0025	2.5
SD-SWIR		0.0246	0.0032	13.0	0.0441	0.0030	6.8	0.1025	0.0025	2.4
SD-MUMM		0.0282	0.0013	4.7	0.0475	0.0012	2.6	0.1053	0.0012	1.1
865 nm		VR-NIR (4,5)	0.0029	0.0006	20.1	0.0053	0.0006	11.0	0.0077	0.0015
	VR-SWIR (5,6)	0.0018	0.0008	43.2	0.0029	0.0008	26.1	0.0300	0.0014	4.7
	VR-SWIR (5,7)	0.0024	0.0010	41.3	0.0035	0.0010	28.0	0.0307	0.0016	5.1
	VR-SWIR (6,7)	0.0044	0.0008	18.0	0.0056	0.0008	13.3	0.0335	0.0014	4.1
	VR-SWIR (6,7) ve	0.0033	0.0014	42.4	0.0045	0.0015	33.0	0.0321	0.0020	6.2
	SD-SWIR	0.0015	0.0014	94.1	0.0022	0.0017	76.7	0.0300	0.0024	7.9
	SD-MUMM	0.0032	0.0009	29.4	0.0043	0.0009	21.3	0.0325	0.0015	4.5

### 3. Results

Fig. 1 shows a subset of the OLI scene of 2014-03-16 over Belgian coastal waters, composited to a 'true colour' RGB image using Rayleigh corrected reflectances from bands 4, 3 and 2. High concentrations of suspended sediments can be seen as bright brownish patches, for example resuspended sediments over the shallow Vlakte van de Raan (51°27' N, 3°24'E), and small scale sediment transport in and around the port of Zeebrugge (51°20'N, 3°12'E). At this spatial resolution (30 m, sharpened using the 15 m panchromatic channel (Vanhellemont & Ruddick, 2014b)), offshore constructions (e.g., the C-Power wind farm at 51°32'N, 2°56'E), large ships and their turbid wakes can be observed. Dumping of dredged sediments at a designated dumping site is visible at 51°21.5'N, 3°16'E (see also Fig. 2). Natural small-scale variability in suspended sediment can also be observed, such as the streaks of sediments related to submarine sand dunes (Du Four & Van Lancker, 2008) on the Vlakte van de Raan (51°28'N, 3°22'E). The small scale

sediment transport around breakwaters can be observed to the east of the port, at 51°21'N, 3°16'E (Fig. 2).

#### 3.1. Validity ranges of the red-NIR and SWIR methods

The same image and subset as in Fig. 1 was processed using the VR-NIR 4,5 and VR-SWIR 6,7 methods. Suspended particulate matter concentration (SPM) is derived from  $\rho_w^4$  using the single band algorithm of Nechad, Ruddick, and Park (2010). Both processors are in good agreement until concentrations of ~30–40  $\text{gm}^{-3}$  (Fig. 3). In regions of higher turbidity, for example on the Vlakte van de Raan (51°27'N, 3°24'E), and west of the harbour of Zeebrugge (51°18'N, 2°56'E), the VR-SWIR method gives much higher SPM values than the VR-NIR method. In these pixels, the assumption in VR-NIR of a linear relationship between  $\rho_w^4$  and  $\rho_w^5$  is invalid – see also Figure 4 of Ruddick, De Cauwer, Park, and Moore (2006) and Doron et al. (2011). At higher turbidities, the  $\rho_w^4$  starts to saturate while  $\rho_w^5$  still linearly increases with turbidity. Thus,

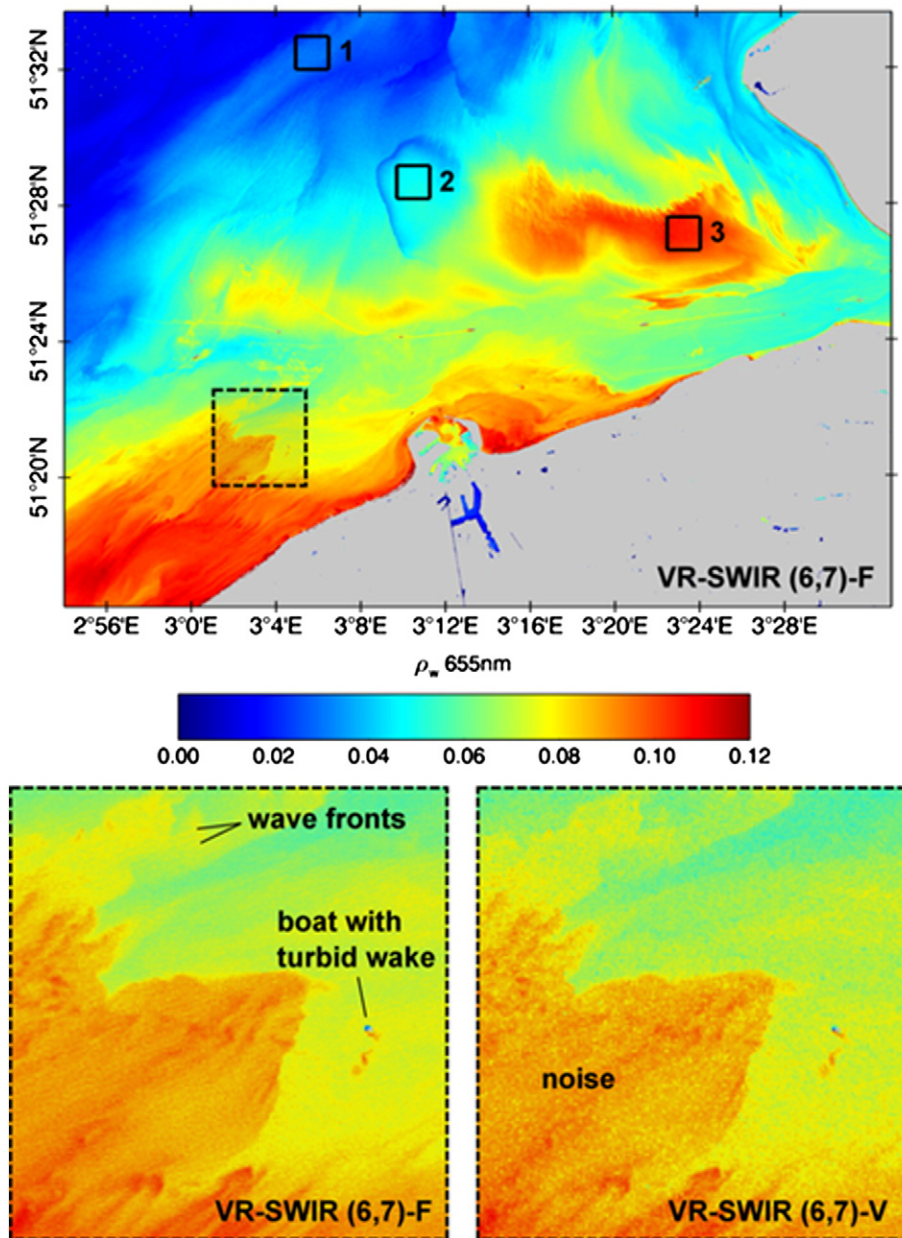


Fig. 7. Water-leaving radiance reflectance at 655 nm ( $\rho_w^4$ ) from the 2014-03-16 image over Belgian coastal waters (2014-03-16, scene LC81990242014075LGN00) processed using VR-SWIR 6,7 with fixed aerosol  $\epsilon$  (top). Numbered boxes show pixels selected for comparison of noise levels in Table 4. Median  $\rho_w$  spectra for these boxes are shown in Fig. 6. The bottom figure shows a detail west of Zeebrugge (dotted box in top figure), with fixed (left) and variable (right) aerosol  $\epsilon$ , illustrating the noise added by using a variable  $\epsilon$ .

using the linear approximation of  $\rho_w^4/\rho_w^5$ ,  $\rho_w^5$  is underestimated. In VR-NIR, this remaining signal in the NIR is then incorrectly attributed to the aerosol multiple scattering reflectance,  $\rho_{am}^5$ . Extrapolation of this overestimated  $\rho_{am}^5$  causes an overcorrection of the red and visible bands. Fig. 4 shows maps of  $\rho_{am}^5$  from both methods, directly estimated in the VR-NIR method, and extrapolated from  $\rho_{am}^7$  in the VR-SWIR method. The largest differences between the methods are correlated to SPM patterns: it is clear that in the highest SPM waters near coast and on the Vlakte van de Raan (51°27'N, 3°24'E), VR-NIR overestimates the aerosol, and underestimates the marine reflectance. For the VR-SWIR method, spatial variability of estimated  $\rho_{am}$  in Fig. 4 is caused mainly by surface features: boats and their short white wakes, wave breaking (51°32'N, 3°24'E), offshore constructions (such as the C-Power wind farm), and a frontal feature (just North of two boats, 51°24'N, 3°12'E), where wave-breaking often occurs at a bathymetric slope.

Similarly, when comparing  $\rho_w$  from VR-NIR and VR-SWIR for bands 1 through 5 (Fig. 5), a good agreement is found at low to moderate reflectances, with the bulk of the points lying on the 1:1 line. At low  $\rho_w^4$  ( $\sim 0.01$ , or SPM  $\sim 3 \text{ g m}^{-3}$ ), VR-SWIR gives reflectances  $\sim 30\%$  higher than VR-NIR, due to a lower estimate of spectral  $\rho_{am}$ . At higher  $\rho_w$  (in any band, e.g.,  $\rho_w^1 \sim 0.05$ ,  $\rho_w^2 \sim 0.07$ ,  $\rho_w^3 \sim 0.10$  or  $\rho_w^4 \sim 0.10$ ), the underestimation of VR-NIR is clear, with a point cloud spread below the 1:1 line. Generally the slopes of the regression are  $< 1$  due to these pixels pulling down the regression line. The two branches in this point cloud correspond to pixels with different sediment characteristics (see below). At high turbidities, the retrieved  $\rho_w^5$  is clearly different between VR-NIR and VR-SWIR, with a much larger range retrieved by the latter. The  $\rho_w^5$  derived using the VR-NIR is quite close to the VR-SWIR, but reaches a saturation around  $\rho_w^5 \sim 0.01$  for turbidity ranges outside the validity range of the linear assumption on the  $\rho_w^4/\rho_w^5$  ratio. An erroneous local minimum is reached at the most turbid and most reflective waters. The median spectrum from three boxes extracted from the 2014-03-16 image is shown in Fig. 6 for the VR-NIR and VR-SWIR methods. Similar performances are found in the relatively clear to moderately turbid waters (boxes 1 and 2), and VR-NIR fails in the extremely turbid waters (box 3). The reasoning behind the pixel selection and the full comparison with other processing settings is given in Section 3.2 and Table 4.

Fig. 5(F) shows the relationship between  $\rho_w^4$  and  $\rho_w^5$  retrieved using the VR-SWIR method, and the linear assumption of VR-NIR (dashed red line,  $\rho_w^4 = 8.7 \cdot \rho_w^5$ ). This plot illustrates that this assumption is valid for  $\rho_w^4$  up to  $\sim 0.06$  (SPM of  $\sim 27 \text{ g m}^{-3}$ ), with increasing underestimation of  $\rho_w^5$  for higher turbidity or reflectance levels. The constant ratio between marine reflectances was thus well suited for the turbidity range in the imagery presented by Vanhellemont and Ruddick (2014a, b), but should be avoided in more turbid waters. It is reassuring that this linear relationship, originally derived from the in situ measurements and theory of Ruddick et al. (2006), can be retrieved directly from Landsat-8 using the VR-SWIR correction that uses no a priori assumptions on the marine reflectance.

The bifurcation at high  $\rho_w$  in Fig. 5 corresponds to the high SPM pixels on the Vlakte van de Raan (lower branch) and west of Zeebrugge (upper branch). Sediments on these locations show different spectral characteristics, and are differently coloured on the RGB composite (Fig. 1). The Vlakte van de Raan sediments have a more reddish hue, while the sediments to the west of Zeebrugge appear brighter and more yellow. For a similar  $\rho_w^5$ , the sediments on the Vlakte van de Raan show a lower  $\rho_w^4$  than those west of Zeebrugge.

### 3.2. Aerosol selection, noise and spatial variability of the aerosol type

Section 3.1 compared products from the atmospheric corrections VR-NIR and VR-SWIR using respectively the (4,5) and (6,7) band combinations, showing the clear superiority of the latter in the more turbid waters. Here, a comparison will be made between all different band combinations for the atmospheric correction, and focusing on the noise levels found in the resulting products.

An image-derived noise estimate is made for each pixel, using the root-mean square difference (RMSD) with the 8 surrounding pixels. This method obviously interprets any spatial variability as being noise, and therefore pixels from regions of apparent spatial uniformity were selected. Three boxes of  $60 \times 60$  pixels were extracted from the imagery, and the median (P50) of the  $\rho_w$  and the RMSD noise estimate were then calculated per box and per band. This pixel selection also allows an absolute comparison of the different methods for different water turbidities. Fig. 7 shows the location of the three boxes in the Belgian coastal zone image, ranging from relatively clear to high turbidities.

#### 3.2.1. Impact of different aerosol correction band combinations on noise

Results from the three boxes are shown in Table 4, with median spectral plots for the VR-NIR and VR-SWIR (6,7) in Fig. 6. The failure of VR-NIR in the turbid box 3 is quite clear, showing very low  $\rho_w$  in the blue (in fact many pixels in the box go negative), and overall large differences compared to the SWIR methods. For the moderately turbid boxes 1 and 2, performances are very similar for the VR-NIR and VR-SWIR methods. VR-NIR retrieves values in between VR-SWIR (5,6/7) and VR-SWIR (6,7). The noise levels are stable per atmospheric correction method over the different boxes, with relative differences then depending on the absolute value of the water reflectance. Lowest noise estimates are found for the VR-NIR and VR-SWIR (6,7). In the most turbid box the performance is very similar across the SWIR methods. Highest noise levels are found for the VR-SWIR (6,7)-V, as a direct result of the noise in the SWIR bands (see further). The low noise in the  $\rho_w^5$  of the VR-NIR method is the result of the calculation of  $\rho_w^5$ : the  $\rho_w^5$  is only used for the determination of the  $\rho_{am}^5$ .  $\rho_w^5$  is calculated as  $\rho_w^4/8.7$ , and thus the noise is  $1/8.7$  of that in  $\rho_w^4$ .

The absolute difference range between the methods is similarly quite stable across the three boxes (Table 5), giving relative differences as a function of the box's turbidity. For example from the most turbid to the clearest box, relative differences are found of 5–14% in  $\rho_w^4$  and 9–57% in  $\rho_w^5$ . The large relative range in  $\rho_w^5$  retrievals is mainly caused by the low overall signal. The differences between the methods can be mainly attributed to the selection of a different aerosol  $\epsilon$  and extrapolation. In fact, this is the sole difference between VR-SWIR (5,7) and VR-SWIR (6,7), the latter with and without variable  $\epsilon$ . Those three methods all assume the same long wavelength aerosol reflectance ( $\rho_{am}^7 = \rho_c^7$ ) but use a different  $\epsilon$  and aerosol extrapolation. It is possible that pixels with non-zero  $\rho_w^5$  are included in the rough clear water selection performed

**Table 5**

The absolute (max–min) and relative (range/max \* 100%) ranges of retrieved  $\rho_w$  across the different “VR” atmospheric correction methods, derived from the median values from the boxes in Fig. 7 and Table 4. In box 3, the VR-NIR method fails (Fig. 3) and the range is given for the VR-SWIR methods alone (\*). Differences between using a fixed and variable  $\epsilon$  in the VR-SWIR (6,7) method are given in the last column.

Band	Box (*) SWIR only	$\rho_w$ range	$\rho_w$ range (relative)	$\Delta\rho_w$ SWIR (6,7) fixed/variable $\epsilon$
443 nm	1	0.0077	20%	0.0029
	2	0.0081	15%	0.0030
	3 (*)	0.0101	16%	0.0028
483 nm	1	0.0067	17%	0.0026
	2	0.0071	11%	0.0027
	3 (*)	0.0088	12%	0.0025
561 nm	1	0.0056	10%	0.0024
	2	0.0059	7%	0.0024
	3 (*)	0.0073	7%	0.0022
655 nm	1	0.0043	15%	0.0019
	2	0.0045	9%	0.0019
	3 (*)	0.0056	5%	0.0020
865 nm	1	0.0026	59%	0.0011
	2	0.0028	49%	0.0012
	3 (*)	0.0034	10%	0.0014

in the VR-SWIR (5,6) and (5,7) methods, artificially inflating the  $\varepsilon$ , and as a result retrieving lower  $\rho_w$ .

### 3.2.2. Impact of spatial smoothing of aerosol type on noise

The absolute differences between the retrieved  $\rho_w$  using a fixed and variable  $\varepsilon$  are stable over the three boxes and all bands ( $\Delta\rho_w$  in Table 5), while the magnitude of the signal changes significantly between boxes 1 and 3 (with a factor  $\sim 3$  in  $\rho_w^4$  and  $\sim 10$  in  $\rho_w^5$ ). In the most turbid box, the difference between the fixed and variable methods is  $\sim 2\%$  in the red, to  $\sim 5\%$  in the blue. These differences are of similar magnitude as the actual noise observed in the image (see absolute and relative RMSD values in Table 4), and are in fact not separable from the noise.

The visual impact of the per-pixel  $\varepsilon$  is quite obvious in the lower panel of Fig. 7. The added noise and along-track scanning artefacts are clearest in the clearest parts, but also in the more turbid parts some fine scale features are less pronounced due to the noise. The three lines running from NE to SW in Fig. 8 are the boundaries of the OLI detectors. The detector boundaries are sometimes visible in the imagery as a result of using a scene-average viewing geometry in the current processing (Franz et al., 2014). The per pixel varying  $\varepsilon^{6,7}$  map is shown in Fig. 8A, and reveals significant noise in the ratio of the two SWIR bands, mainly caused by (1) the low SWIR signal, giving large relative changes for a small absolute difference, and (2) inherent noise in the SWIR bands. Spatial smoothing of the SWIR bands has been applied to MODIS data

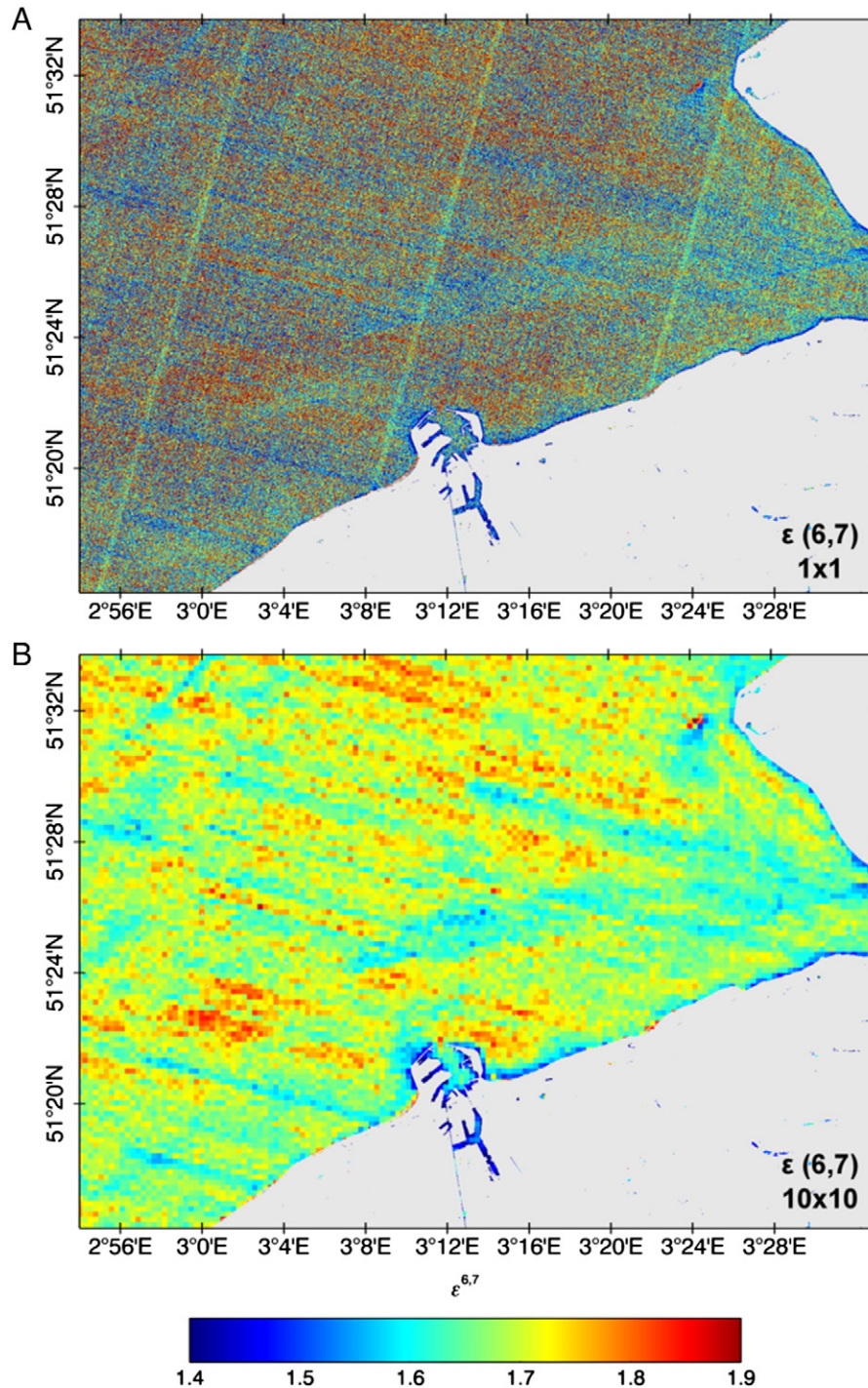


Fig. 8. Comparison of the per-pixel aerosol  $\varepsilon^{6,7}$  from the 2014-03-16 image over Belgian coastal waters at native resolution (top) and after averaging  $10 \times 10$  pixels (bottom)  $\varepsilon$ .

to reduce the noise (Wang & Shi, 2012), and proposed for OLI data (Pahlevan et al., 2014). For this OLI image, resampling to  $10 \times 10$  pixels ( $\sim 300$  m) does not fully remove the noise in the image, but does reveal some spatial features including sensor artefacts (Fig. 8B). A further analysis of smoothing the  $\varepsilon$  fields and using a single  $\varepsilon$  per (sub-)scene is given in Supplementary data 1. For the scenes presented here,  $\varepsilon$  was found to be reasonably stable over the scene, and using a single scene median value is deemed appropriate (with differences in  $\rho_w < 5\%$  for turbid waters). Even with uniform aerosol type,  $\varepsilon$  is expected to vary spatially in reality because of multiple-scattering effects, but this is very small at the scale of an OLI tile ( $\sim 170$  by  $185$  km)

### 3.2.3. Impact of selecting aerosol type over clear waters

Next, the aerosol type ( $\varepsilon$ ) selection between the different methods is compared. Only one method presented here, VR-SWIR (6,7)-V, uses a per-pixel  $\varepsilon$  estimation. The other methods use an aerosol type fixed per scene, but the value of  $\varepsilon$  is estimated at different wavelengths and over different pixels. VR-SWIR (6,7) estimates the  $\varepsilon$  over all water pixels, while VR-NIR and VR-SWIR (5,6) and (5,7) first detect clear waters where the NIR marine signal can be ignored. The former uses an iterative method, while the others select pixels based on spectral relationships in  $\rho_c$  (see Methods). For each method, the  $\varepsilon$  is then extrapolated from the longest wavelength to the other bands using an exponential function (Eqs. 6 and 7). A comparison of  $\rho_{am}$  normalized to  $\rho_{am}^5$  is shown in Fig. 9. Differences in the normalized  $\rho_{am}$  between the methods are relatively low in the red,  $\sim 15\%$ , and reach  $\sim 32\%$  in the shortest blue band. These ranges are similar to the ranges in the retrieved  $\rho_w$  (Table 5), illustrating directly the importance of correct  $\varepsilon$  determination. Smallest differences are found between the SWIR methods using the same longest waveband. The atmospheric correction of highly turbid waters will be relatively insensitive to these differences in  $\varepsilon$ , as the marine signal is very strong compared to the aerosol reflectance, and this uncertainty has a relatively low impact on the derived  $\rho_w$  (Eqs. 5, 10). This is also shown by the decrease of relative differences between the methods from the clear to turbid box (relative  $\rho_w$  range in Table 5). For the SWIR methods, the  $\varepsilon$  was also calculated for clear water pixels, determined as pixels where  $\rho_w^4 < 0.015$  after a first automated processing using VR-SWIR (6,7)-F. Small differences are found when comparing the  $\varepsilon$  derived over the full scene and over the clear waters. VR-SWIR (6,7)-F shows spectral  $\varepsilon$  changes of  $< 1\%$  from the red to the blue, VR-SWIR (5,6)  $\sim 1\text{--}3\%$  and VR-SWIR (5,7)  $\sim 1\text{--}2\%$  (Fig. 9B). Larger differences are found when restricting to even clearer water pixels (e.g.,  $\rho_w^4 < 0.005$ ), but those pixels are not uniformly present over the scene. Moreover, marine reflectances – even offshore – are

often higher in the southern North Sea. The aerosol properties, as well as the distribution of clear water pixels, seem to be quite uniform over this scene, with the main difficulty being to accurately determine the median aerosol type.

### 3.2.4. Comparison with SeaDAS processing

By means of illustration and quick intercomparison, the images were also processed using the SeaDAS software, in which the L8/OLI processing will be publicly available soon (Franz et al., 2014). Overall very good agreements are found, with similar ranges of  $\rho_w$  retrieved by SeaDAS and our processing. Slightly higher retrievals are found in the green, especially in the more turbid pixels. Noise levels are also comparable, with, as expected, highest noise levels in the blue. The lowest relative noise levels are found in the most turbid pixels for the red and green channels. The processor with a per-pixel variable aerosol model (SD-SWIR) shows large noise, especially in the clearest box and towards the blue end of the spectrum. Higher noise is found for SD-SWIR than for VR-SWIR (6,7)-V, because the former will not only vary  $\varepsilon$  per pixel, but also the model used for the aerosol extrapolation, which is constrained to exponential in VR-SWIR (6,7)-V. Large differences between the relative noise values are found for both methods, due to higher absolute RMSD values in the SD-SWIR dataset, with lower absolute median marine reflectances.

### 3.3. Comparison with MODIS data

Insufficient quality controlled in situ data is currently available for the validation of our OLI atmospheric correction. Therefore, a comparison is made between the red and NIR bands on OLI (655 and 865 nm) with the high resolution (250 m) MODIS land bands (645 and 859 nm). SWIR bands are used for atmospheric correction: the 1609 and 2201 nm bands for OLI, and the 1240 and 2130 nm bands for MODIS. For cloud-free images with a large range of marine reflectances, a good correspondence between MODIS and OLI is found for the Belgian coastal zone, both in spatial features and absolute retrievals (Figs. 10 and 11 and Supplementary data 2). Data from MODIS-Terra is not truly independent from MODIS-Aqua data, and its use in ocean colour applications should be considered carefully. However, it is included in the comparison here as the time difference between Aqua and Landsat-8 overpasses is significant in these tidal coastal waters.

The comparison for 2014-03-16 is shown in Fig. 10 for the red and Fig. 11 for the NIR bands. A good correspondence in terms of absolute values and spatial patterns is found with MODIS-Terra (time difference: 35 min), with some significant along-track striping on the Terra image.

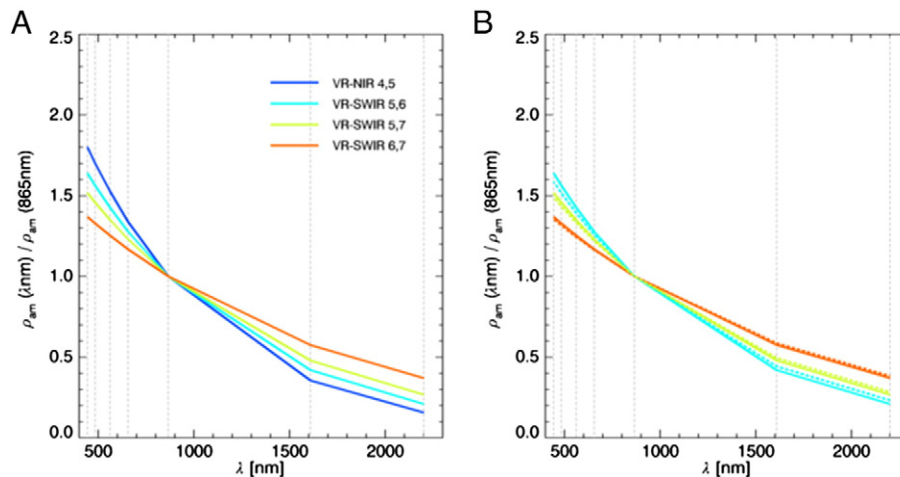


**Fig. 9.** Comparison of the estimated aerosol reflectance ( $\rho_{am}$ ) normalized to  $\rho_{am}^5$  for the Belgian coastal zone image (2014-03-16, scene LC81990242014075LGN00). Left: using the pixel selection described in Section 2, and right: the SWIR based processors, using the standard pixel selection (solid lines), and using clear water pixels ( $\rho_w^4 < 0.015$ ) selected after processing using VR-SWIR (6,7)-F (dashed lines). Vertical dashed lines show the OLI band centres. The solid and dashed lines on the right plot are almost superimposed, showing that  $\varepsilon$  is quite stable over the scene.

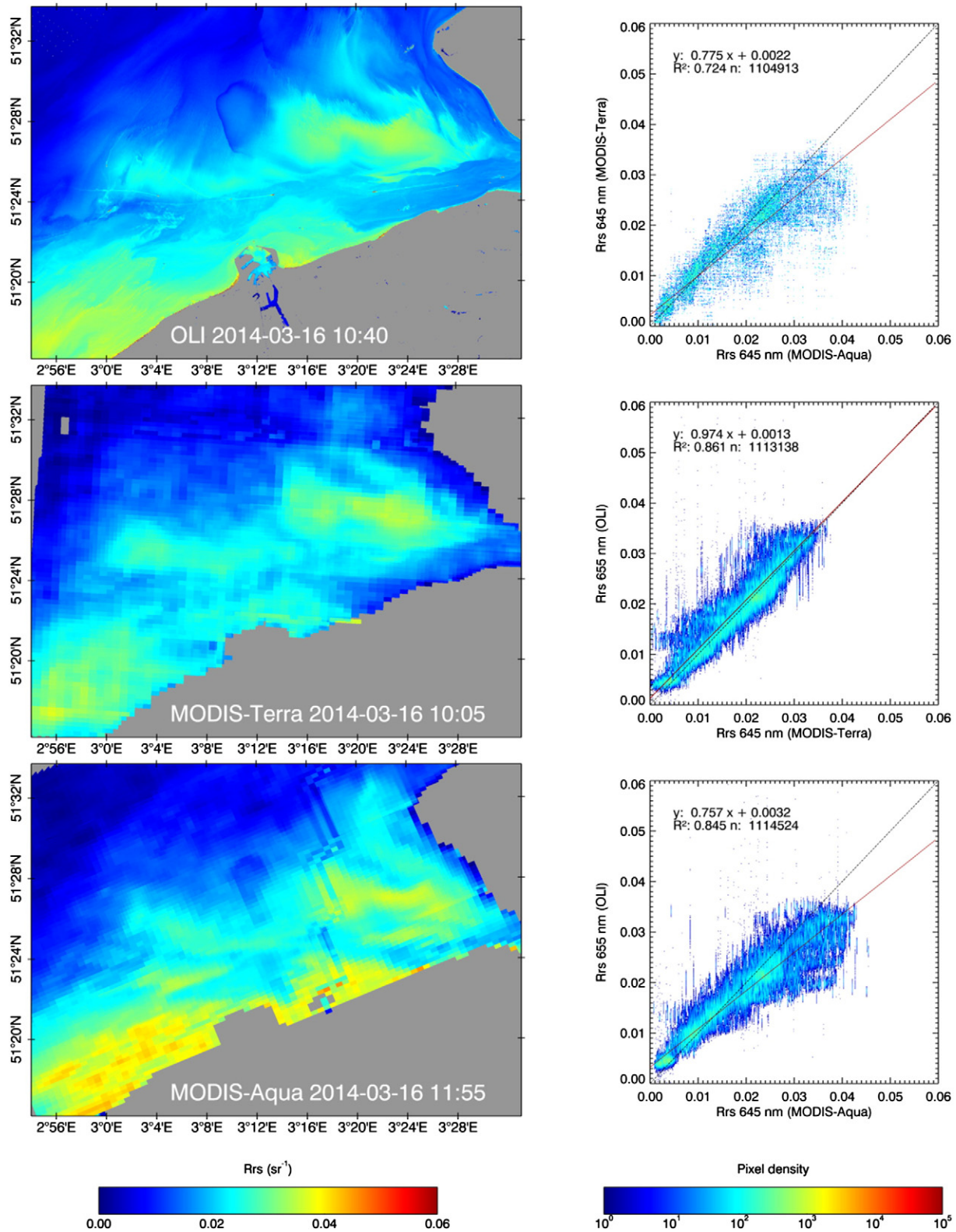


**Fig. 10.** Comparison of red remote sensing reflectances ( $Rrs = \rho_w/\pi$ ) for the Belgian coastal zone on 2014-03-16 derived from (top) OLI 655 nm at 10:40 UTC (scene LC81990242014075LGN00), (middle) MODIS-Terra 645 nm at 10:05UTC and (bottom) MODIS-Aqua 645 nm at 11:55 UTC. The scatter plots show the comparison between (top) MODIS-Aqua and MODIS-Terra, (middle) MODIS-Terra and OLI and (bottom) MODIS-Aqua and OLI. Colours denote pixel densities, the dashed black line is the 1:1 line, and the red line is the Reduced Major Axis (RMA) regression line.

Largest differences are found between OLI and MODIS-Aqua (time difference: 1 h 15 min), but this is to be expected in a region with large tidal dynamics (Vanhellemont, Neukermans, & Ruddick, 2014). Higher

reflectances are observed by MODIS-Aqua in the near-coast sediments, both in the red and NIR bands. Similar and larger differences are found when comparing MODIS-Aqua and MODIS-Terra (time difference: 1 h

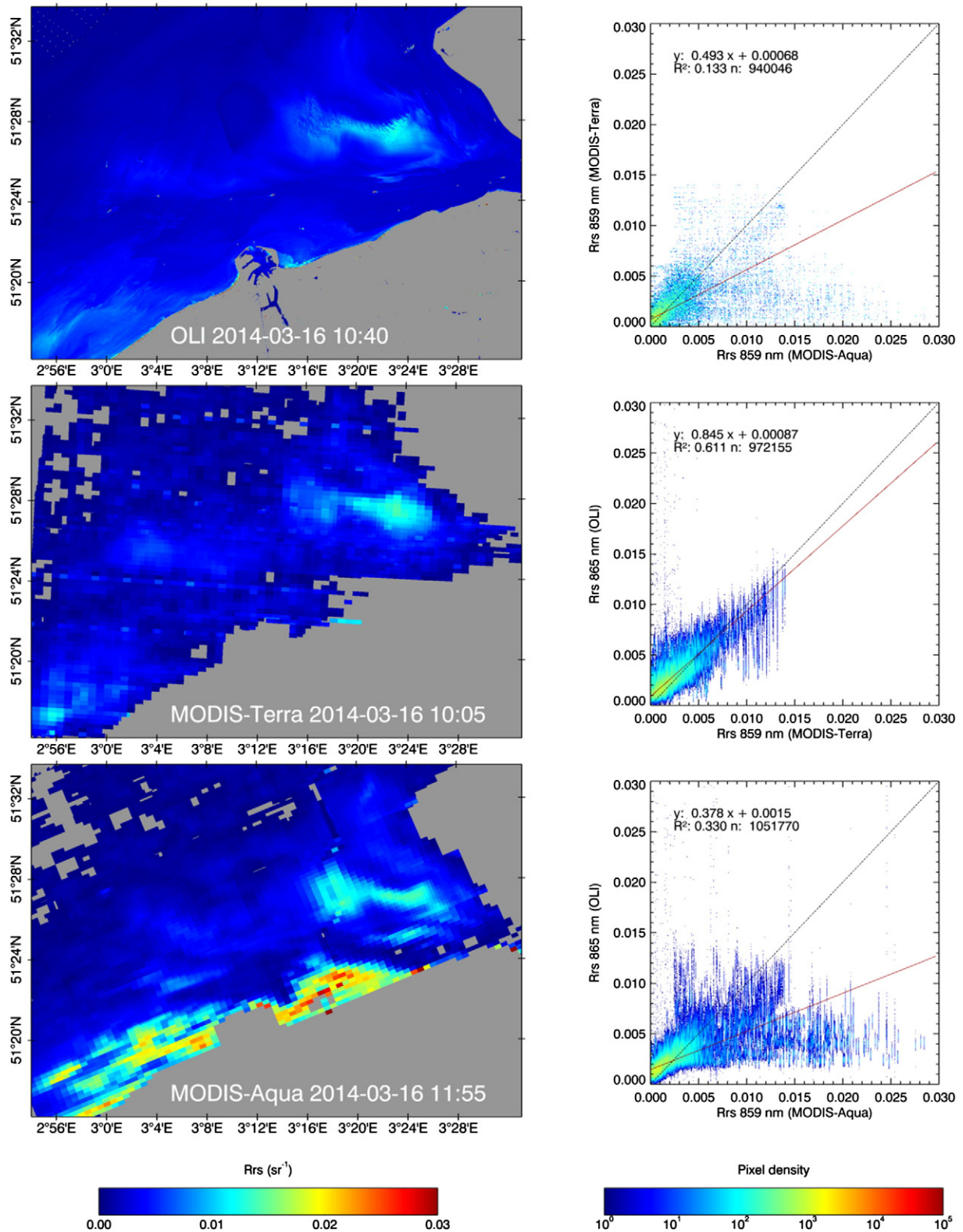


**Fig. 11.** Comparison of NIR Remote sensing reflectances ( $Rrs = \rho_w/\pi$ ) for the Belgian coastal zone on 2014-03-16 derived from (top) OLI 865 nm at 10:40UTC (scene LC81990242014075LGN00), (middle) MODIS-Terra 859 nm at 10:05UTC and (bottom) MODIS-Aqua 859 nm at 11:55 UTC. The scatter plots show the comparison between (top) MODIS-Aqua and MODIS-Terra, (middle) MODIS-Terra and OLI and (bottom) MODIS-Aqua and OLI. Colours denote pixel densities, the dashed black line is the 1:1 line, and the red line is the Reduced Major Axis (RMA) regression line.

50 min). Further comparisons for 2013-10-07, 2013-12-10, 2014-02-03, and 2014-04-01 are given in Supplementary data 2, showing good performances for various sun angles and sediment concentrations.

The best fit line in the OLI-MODIS comparison has a slope different from 1 due to temporal variability, but there is quite some scatter around this line. Much of the scatter can be attributed to the noise in

the MODIS images and to the large difference in spatial resolution between MODIS (250 m) and OLI (30 m). The vertical stripes in the scatterplot of OLI vs MODIS represents the range of OLI values for a single MODIS value (pixel). The reprojection of the MODIS swath to the OLI image is a potential additional source of noise: there are obvious along-track oriented artefacts in the resampled MODIS image. Significant noise is found in the MODIS images as a result of the low SNR in the SWIR bands (Werdell et al., 2010), and the sensor radiometric degradation over the past decade. Some effects of the bow-tie effect (overlapping scan-lines) can also be observed as the sub-scenes are quite close to the edge of swath. Due to the orbits of the satellites, no centre of swath MODIS data is available for the Landsat-8 overpasses in this region. There are spectral differences between the bands, but they are assumed to cause effects small in comparison with the ones mentioned above.

### 3.4. Automatic detection of high concentrations of black sediments

Due to the low noise and the high spatial resolution of the OLI bands and the accurate atmospheric correction now possible over turbid waters, new applications can be developed using Landsat-8 data. As example, we propose a simple method to automatically detect and flag high concentrations of black suspended sediments.

Offshore dumping of sediments dredged from harbours in Belgian coastal waters has been previously observed on Landsat-8 imagery by Vanhellemont and Ruddick (2014b). On an RGB composite (e.g., Fig. 13) these sediments have a characteristic dark or even black colour. The dark colour could indicate strong absorption, either from CDOM, found e.g. along the Florida coast (Hu, Muller-Karger, Vargo, Neely, & Johns, 2004), or from highly absorbing particles. In the current section we develop a method to detect such absorbing particles as distinct from CDOM.

After performing the atmospheric correction described above, marine reflectances in the visible channels are, as expected, lower for these dark pixels than the ambient values. The NIR reflectance however, is quite high, even exceeding the validity limits ( $\rho_w^5 > 0.06/8.7$ ) of the VR-NIR method. Additionally, the spectral relationship between  $\rho_w^4$  and  $\rho_w^5$  for these sediments is very different from what is assumed by VR-NIR.

With a simple test on the marine reflectances, these high concentrations of black sediments can be automatically detected by checking whether:

- the NIR marine reflectance is greater than a threshold for turbid waters:

$$\rho_w^5 > 0.01 \quad (13)$$

- and, the maximum marine reflectance in three visible bands is low for this turbidity:

$$\max(\rho_w^2, \rho_w^3, \rho_w^4) < 0.07 \quad (14)$$

- and with an additional constraint for turbid atmospheres:

$$\rho_{am}^5 < 0.012. \quad (15)$$

The first test (13) removes cases where absorption is caused by CDOM rather than suspended sediments. From the theory and measurements of Ruddick et al. (2006) and our own image processing, we can assume that at the upper validity range of the VR-NIR processing (at around  $\rho_w^5 \sim 0.06/8.7 \sim 0.007$ ),  $\rho_w^4$  will be  $\sim 0.06$ . Fig. 5F shows that for the NIR threshold taken here,  $\rho_w^5 = 0.01$ ,  $\rho_w^4$  will typically range between  $\sim 0.05$  and  $\sim 0.08$ , and that  $\rho_w^4$  will increase (albeit not linearly)

with increasing  $\rho_w^5$ . Furthermore, marine reflectances in this region are often higher at 561 nm than at 655 nm ( $\rho_w^3 > \rho_w^4$ ), see for example data ranges on the abscissa in Fig. 5C and D. The maximum visible reflectance (14) will thus be  $> \rho_w^4$ , in most cases. The black sediment flag can be easily represented on a scatterplot of this maximum visible reflectance as a function of NIR reflectance (Fig. 12). Samples of automatically detected black sediment plumes are shown in Fig. 13. Some false positives are retrieved in cloud shadows, object shadows (boats, constructions), and undetected sub-pixel scale objects.

## 4. Discussion

Imagery from the turbid Belgian coastal waters is presented from the first operational year of Landsat-8, showing realistic spatial distribution of marine and atmospheric features for a range of different SPM concentrations and sun angles. The magnitude and spatial patterns of red and NIR  $\rho_w$  retrieved with OLI are well correlated with observations from MODIS Aqua and Terra, processed in SeaDAS using a SWIR based aerosol selection. Some differences are found in the absolute retrievals, but these can be largely attributed to changes in water turbidity due to variability between the acquisition times for the two sensors. This is also clear from a direct comparison of MODIS-Aqua and MODIS-Terra (top right scatterplots in Figs. 10 and 11), which follow common calibration and processing schemes. This difference is mainly due to time difference, as shown in previous papers that discuss short term variability using in situ data and geostationary imagery (Neukermans, Ruddick, & Greenwood, 2012; Vanhellemont, Neukermans, et al., 2014). Worse agreements are found for images with low reflectances (typically summer images): the correlation statistics are bad due to the low range of values in the datasets. Not all images provided satisfactory results in the inter-comparison, with the most important causes being, (1) the lack of corresponding pixels as a result of moving and patchy clouds, (2) low reflectance ranges caused by low concentrations of suspended sediments, impacting correlation statistics, and (3) the coarse resolution of MODIS with respect to OLI, and some obvious sensor artefacts and noise in the MODIS data.

It is clear that the assumption of a linear relationship between  $\rho_w^4$  and  $\rho_w^5$  is only valid up to moderate turbidities. At higher turbidities,  $\rho_w^4$  saturates while  $\rho_w^5$  keeps increasing with turbidity (Doron et al., 2011; Ruddick et al., 2006). Due to this saturation in highly turbid waters, the VR-NIR method will underestimate the  $\rho_w^5$  and thus  $\rho_{am}^5$  will

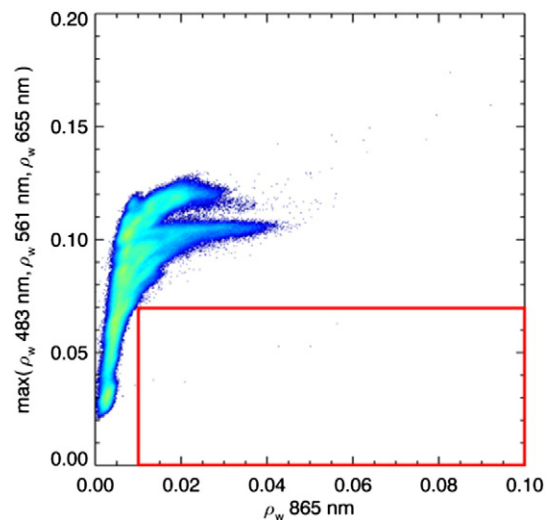


Fig. 12. Scatterplot showing maximum marine reflectance at 483, 561 and 655 nm [ $\max(\rho_w^2, \rho_w^3, \rho_w^4)$ ] as function of marine reflectance at 865 nm, over Belgian waters for image LC81990242014075LGN00. The red box shows where the flag for high concentrations of black sediments would be triggered.

be overestimated, leading to an overcorrection in the visible bands (1–4). Some of the spatial patterns in the VR-NIR  $\rho_{am}^5$  are clearly correlated to turbid marine features (Fig. 4). The new VR-SWIR atmospheric correction presented here allows for an independent and uncorrelated estimation of  $\rho_{am}^5$  and  $\rho_w^5$ , and shows that for typical sediments the assumption in the previous VR-NIR method is valid up to  $\rho_w^4 \sim 0.06$  or SPM  $\sim 27 \text{ g m}^{-3}$ .

The different band combinations for the SWIR-based atmospheric correction (bands 5,6; 5,7; 6,7) offer a very similar performance in  $\rho_w$  estimation. Absolute differences between the methods range from  $\sim 0.004$  for  $\rho_w^5$ ,  $\sim 0.006$  for  $\rho_w^4$ ,  $\sim 0.007$  for  $\rho_w^3$ ,  $\sim 0.009$  for  $\rho_w^2$ , and  $\sim 0.010$  for  $\rho_w^1$  (Table 5). The relative value depends on the pixel brightness, for the turbid box 3 in Fig. 7 for example, these values represent relative differences of  $\sim 5\%$  in the red up to  $\sim 20\%$  in the blue. Differences between the methods are mainly caused by a different median aerosol type selection. For example, VR-SWIR (5,7) and (6,7) assume the same multiple scattering aerosol reflectance ( $\rho_{am}^7 = \rho_c^7$ ) but retrieve different  $\rho_w$  due to a different aerosol type. Typically, VR-SWIR (6,7) retrieves lower  $\epsilon$  values than VR-SWIR (5,7), causing higher  $\rho_w$  retrievals. This is potentially due to the inclusion of pixels where  $\rho_w^5 \neq 0$  in the clear water pixel selection, inflating the  $\epsilon$  value of the SWIR methods using the NIR band as shortest wavelength. However, when selecting clear water pixels after a first processing using VR-SWIR (6,7), only small differences in computed  $\epsilon$  are found, resulting in differences  $< 4\%$  in the shortest blue band.

A distinct advantage of using the 6,7 band pair is that no clear water pixels are necessary to determine the aerosol type. In other methods, an automatic  $\epsilon$  estimation is practically impossible when there are no bands where  $\rho_w = 0$ , for example when no clear water pixels are present in the image. Additionally, no errors are introduced by performing an automatic per-image clear water pixel selection, where including turbid pixels could influence the aerosol type determination. Spatially fixed and per-pixel variable aerosol types were evaluated for OLI, as the SWIR bands can be assumed black over all water pixels. A pixel-by-pixel  $\epsilon$  estimation using the 6,7 band pair introduces additional noise in the end products, while showing no significant absolute differences in the retrievals. For the images presented here, the variability of  $\epsilon$  per pixel was of the order of – and in fact not separable from – the noise introduced by using the ratio of the SWIR bands as per-pixel  $\epsilon$ . Noise was obvious in the end products, especially over clearer waters, and some small scale marine features present in the visible channels were smudged by the noise. A noise estimation is made for the different methods, including the per pixel variable epsilon, for relatively homogeneous boxes in the image. Absolute noise levels are stable over various turbidity levels, leading to a decrease of relative noise with reflectance. By using a fixed  $\epsilon$  per scene, differences on the resulting  $\rho_w$  are small ( $\sim 2\%$  to  $\sim 5\%$  from the red to the blue in turbid waters), while strongly reducing the noise due to the strong signal and high SNR in the VIS and NIR bands. For the scenes presented here, the variability of  $\epsilon$  from pixel to pixel is likely lower than the noise in the ratio of the SWIR bands. Better performance is reached when smoothing the  $\epsilon$  dataset, or by selecting a sub-scene fixed  $\epsilon$  (Supplementary data 1). Further research on reducing noise in the SWIR bands, e.g., by spatial binning is advised. In some cases good results over turbid waters can be obtained without SWIR bands (Supplementary data 1). For example, when clear water pixels are present in the sub-scene, and when both aerosol type ( $\epsilon$ ) and aerosol path reflectance ( $\rho_{am}$ ) can be considered stable over the scene, the aerosol correction can be computed as the median  $\epsilon$  and  $\rho_{am}$  over the clear water pixels. However, the aerosol concentration does often vary significantly in space, and for many (coastal) regions and scenes the assumption of a fixed  $\rho_{am}$  is invalid. Furthermore, this technique again depends on the presence of clear water pixels in the sub-scene of interest, which can be altogether avoided by using a SWIR based atmospheric correction.

Different sediment types are observed that show different relationships between  $\rho_w^4$  and  $\rho_w^5$  at high turbidities, where  $\rho_w^4$  starts to saturate. In some images, black sediment patches are detected, where the reflectance of the visible bands is low due to the high absorption of the

sediments. The automatic detection and flagging of high concentration of these black suspended sediments (for example, those dumped by dredging ships) is feasible using a relatively simple test after the SWIR based atmospheric correction. Inclusion errors are made for some pixels near cloud shadows, and on the shoreline under cloud shadow, that are spectrally similar to the black sediments (Fig. 13B). These could be filtered out with a good cloud shadow detection (e.g., Zhu & Woodcock, 2012). Some cases, such as solitary erroneously flagged pixels, could be removed using standard image processing techniques, such as an erosion filter or a buffer around the land/cloud masks. With a low enough sun, the test also triggers for shadows cast on the sea surface by vessels and offshore structures. These pixels can be excluded by buffering on the land/cloud mask (that includes objects on the sea surface), or by object shadow detection taking into account sun location. Not all dumped material is detected with this threshold based test, not even within the same event, as settling of particles and different mixing concentrations of water and the dumped material results in changes in  $\rho_w^5$ . The pixels masked in black in Fig. 13B, for example, have a lower than usual visible reflectance, but the  $\rho_w^5$  has returned to background levels, and so are not picked up due to the threshold on  $\rho_w^5$ . This also suggests that the dredged and dumped material may be a mixture of dissolved organic matter (from microbial breakdown of organic matter, potentially adsorbed to the sediment particles at the time of dredging and dumping) and sediments, rather than just a high concentration of absorbing sediments. The turbid water threshold used here ( $\rho_w^5 > 0.01$ ) is fixed, and not directly related to the concentrations within the sediment plumes that can obviously vary significantly. A number of independent dumping events have been detected (Fig. 13). Performance of the test applied to the full archive of coastal Landsat-8 images needs to be evaluated.

## 5. Conclusions

By extending the previous atmospheric correction to extremely turbid waters, this study further illustrates the excellent capabilities of Landsat-8 for monitoring of coastal and estuarine waters. The advantages of the high resolution of L8/OLI for coastal applications are clear: the images are at a spatial resolution where human impacts are obvious. Many human activities take place in coastal and estuarine waters, where a turbid water atmospheric correction is often needed. European countries are required to monitor coastal and inland waters for the Water Framework Directive (WFD) and the Marine Strategy Framework Directive (MSFD).

The atmospheric correction presented here uses the SWIR bands to independently derive marine and aerosol reflectances in the NIR. No assumptions on the marine reflectances are made, but realistic relationships are retrieved. The spatial distribution and magnitude of the retrieved marine reflectance are uncorrelated with the estimated aerosol reflectance. In absolute terms, products compare well with those from the MODIS SWIR based atmospheric correction. The intercomparison shows high variability of marine reflectances both in space and time. Very good results are retrieved for extremely turbid waters, with improved resolution and noise levels in comparison with MODIS on the Aqua and Terra platforms. The latter sensors however, offer a daily revisit time at moderate latitudes, in contrast with the 16-day track repeat of Landsat-8. In general, the use of the two SWIR bands for the aerosol correction over turbid waters is preferred, with a sub-scene or other locally representative, but fixed, epsilon value.

Using Landsat-8 and the SWIR-based atmospheric correction, it is possible for the first time to detect different particle types in (extremely) turbid waters from space: with increasing  $\rho_w^5$ , and thus turbidity, we observe different saturation levels of  $\rho_w$  in the visible bands. These different saturation levels can be linked to separate features in the water, often distinctly coloured on the RGB composite. The reflectance at which these pixels saturate is related to specific inherent optical properties of the suspended particles, the investigation of which is a follow-up to this work. As first

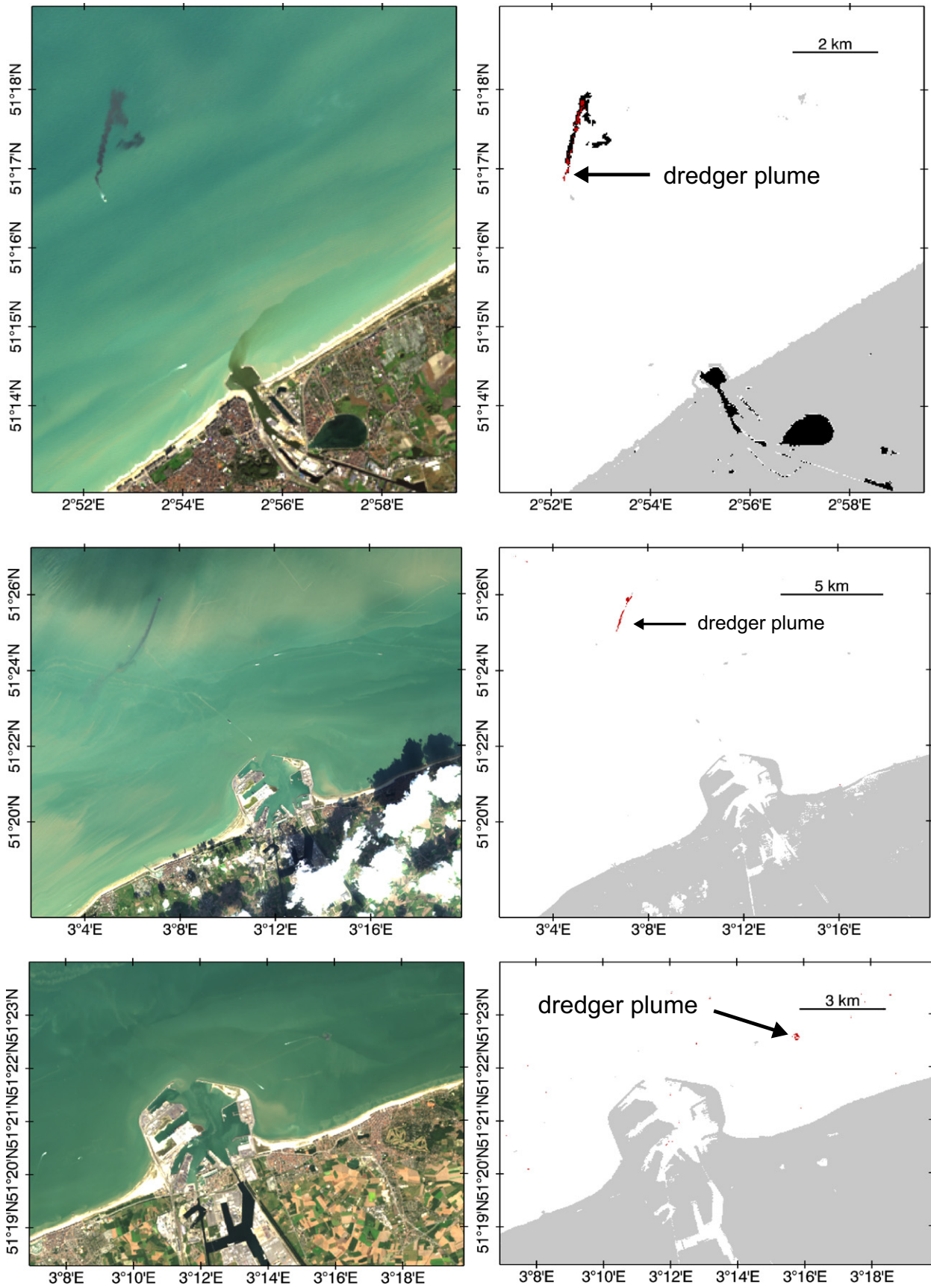


**Fig. 13.** Ships dumping dredged matter offshore observed with Landsat-8, Top: Oostende, 2013-10-30 at 10:47 UTC (scene LC82000242013303LGN00). Middle: Zeebrugge, 2013-10-07 at 10:41 UTC (scene LC81990242013280LGN00). Bottom: Zeebrugge on 2013-09-05 at 10:42 UTC (scene LC81990242013248LGN00). Left column: Rayleigh corrected RGB (channels 4–3–2) image showing the black colour of the dredged material. Right column: masking in red where the turbidity threshold on  $\rho_w^5$  is reached, and the maximum visible reflectance is low (see text for details). The top image is also masked with black when the maximum visible reflectance is low, but where  $\rho_w^5 > 0.001$  (~background turbidity at the ship location), to show where the turbidity in the plume has returned to ambient values.

example we have demonstrated here a prototype detection algorithm for black suspended sediments, e.g., from dredging and dumping operations. Such a flag has obvious interest for coastal zone managers, but, as the dredger plumes are extremely turbid, only becomes realistic with high quality SWIR bands and a SWIR-based atmospheric correction.

The USGS free data policy and the good SNR of L8/OLI data (compared to previous Landsat missions) make this a very attractive new source of data for coastal and estuarine sediment transport studies. In particular, the SWIR bands on L8/OLI offer an impressive SNR, even at native resolution, and are likely the best SWIR bands currently in space. This facilitates the adoption of a robust, low noise SWIR-based aerosol correction, as demonstrated here, and provides an indication of the advantages that could be achieved for turbid waters with well-specified SWIR bands on future ocean colour sensors. A better SNR for the SWIR bands would improve further performance for open ocean waters where aerosols vary in space. Including SWIR bands on a sensor is expensive, but is necessary to extend the usefulness of the sensor by improving the monitoring of turbid coastal and inland waters. Even the inclusion of one SWIR band in addition to a NIR band – the latter a common feature on many sensors – allows for a robust atmospheric correction if the aerosol type can be determined for clear water pixels. A number of existing and upcoming satellites have SWIR bands on board, offering new opportunities for remote sensing of turbid coastal waters; for example, VIIRS has 3 SWIR bands similar to those of MODIS, the European Sentinel-2/MSI will have 2 SWIR bands (1610 and 2190 nm), Sentinel-3 will have 1 on OLCI (1020 nm) and 2 on SLSTR (1610 and 2250 nm). The commercial Worldview-3 (launched August 13, 2014) even has 8 SWIR bands (1195 to 2365 nm).

## Acknowledgements

This work was funded by the European Community's Seventh Framework Programme (FP7/2007–2013) under grant agreement n° 606797 (HIGHROC project). USGS and NASA are thanked for the Landsat-8 imagery. NASA is thanked for the MODIS Aqua/Terra imagery and the SeaDAS processing software. Students and professors at the IOCCG summer school 2014 are thanked for beta-testing the processor described here for various regions around the world. Three anonymous reviewers are thanked for their thorough reading of the manuscript and their helpful comments.

## Appendix A. Supplementary data

Supplementary data to this article can be found online at <http://dx.doi.org/10.1016/j.rse.2015.02.007>.

## References

- Bailey, S.W., Franz, B.A., & Werdell, P.J. (2010). Estimation of near-infrared water-leaving reflectance for satellite ocean color data processing. *Optics Express*, 18, 7521–7527.
- Doron, M., Bélanger, S., Doxaran, D., & Babin, M. (2011). Spectral variations in the near-infrared ocean reflectance. *Remote Sensing of Environment*, 115, 1617–1631.
- Du Four, I., & Van Lancker, V. (2008). Changes of sedimentological patterns and morphological features due to the disposal of dredge spoil and the regeneration after cessation of the disposal activities. *Marine Geology*, 255, 15–29.
- Franz, B.A., Bailey, S.W., Kuring, N., & Werdell, P.J. (2014). Ocean color measurements from Landsat-8 OLI using SeaDAS. *Proc. Ocean Optics 2014, Portland Maine (USA)*, 26–31 October 2014.
- Gordon, H.R., & Wang, M. (1994). Retrieval of water-leaving radiance and aerosol optical thickness over the oceans with SeaWiFS: A preliminary algorithm. *Applied Optics*, 33, 443–452.
- Goyens, C., Jamet, C., & Ruddick, K. (2013). Spectral relationships for atmospheric correction. II. Improving NASA's standard and MUMM near infra-red modeling schemes. *Optics Express*, 21, 21176–21187.
- Goyens, C., Jamet, C., & Schroeder, T. (2013). Evaluation of four atmospheric correction algorithms for MODIS-Aqua images over contrasted coastal waters. *Remote Sensing of Environment*, 131, 63–75.
- Hu, C., Carder, K.L., & Muller-Karger, F.E. (2000). Atmospheric correction of SeaWiFS imagery over turbid coastal waters: A practical method. *Remote Sensing of Environment*, 74, 195–206.
- Hu, C., Feng, L., Lee, Z., Davis, C.O., Mannino, A., McClain, C.R., et al. (2012). Dynamic range and sensitivity requirements of satellite ocean color sensors: Learning from the past. *Applied Optics*, 51, 6045–6062.
- Hu, C., Muller-Karger, F.E., Vargo, G.A., Neely, M.B., & Johns, E. (2004). Linkages between coastal runoff and the Florida Keys ecosystem: A study of a dark plume event. *Geophysical Research Letters*, 31.
- Irons, J.R., Dwyer, J.L., & Barsi, J.A. (2012). The next Landsat satellite: The Landsat Data Continuity Mission. *Remote Sensing of Environment*, 122, 11–21.
- Jiang, L., & Wang, M. (2014). Improved near-infrared ocean reflectance correction algorithm for satellite ocean color data processing. *Optics Express*, 22, 21657–21678.
- Knaeps, E., Dogliotti, A., Raymaekers, D., Ruddick, K., & Sterckx, S. (2012). *In situ* evidence of non-zero reflectance in the OLCI 1020 nm band for a turbid estuary. *Remote Sensing of Environment*, 120, 133–144.
- Kou, L., Labrie, D., & Chylek, P. (1993). Refractive indices of water and ice in the 0.65- to 2.5- $\mu$ m spectral range. *Applied Optics*, 32, 3531–3540.
- Moore, G., Aiken, J., & Lavender, S. (1999). The atmospheric correction of water colour and the quantitative retrieval of suspended particulate matter in Case II waters: Application to MERIS. *International Journal of Remote Sensing*, 20, 1713–1733.
- Morel, A., & Gentili, B. (1996). Diffuse reflectance of oceanic waters. III. Implication of bidirectionality for the remote-sensing problem. *Applied Optics*, 35, 4850–4862.
- Nechad, B., Ruddick, K., & Park, Y. (2010). Calibration and validation of a generic multisensor algorithm for mapping of total suspended matter in turbid waters. *Remote Sensing of Environment*, 114, 854–866.
- Neukermans, G., Ruddick, K., Bernard, E., Ramon, D., Nechad, B., Deschamps, P.-Y., et al. (2009). Mapping total suspended matter from geostationary satellites: A feasibility study with SEVIRI in the Southern North Sea. *Optics Express*, 17, 14029–14052.
- Neukermans, G., Ruddick, K., & Greenwood, N. (2012). Diurnal variability of turbidity and light attenuation in the southern North Sea from the SEVIRI geostationary sensor. *Remote Sensing of Environment*, 124, 564–580.
- Nordkvist, K., Loisel, H., & Gaurier, L.D. (2009). Cloud masking of SeaWiFS images over coastal waters using spectral variability. *Optics Express*, 17, 12246–12258.
- Pahlevan, N., Lee, Z., Wei, J., Schaaf, C.B., Schott, J.R., & Berk, A. (2014). On-orbit radiometric characterization of OLI (Landsat-8) for applications in aquatic remote sensing. *Remote Sensing of Environment*, 154, 272–284.
- Ruddick, K., De Cauwer, V., Park, Y.-J., & Moore, G. (2006). Seaborn measurements of near infrared water-leaving reflectance: The similarity spectrum for turbid waters. *Limnology and Oceanography*, 51, 1167–1179.
- Ruddick, K.G., Ovidio, F., & Rijkeboer, M. (2000). Atmospheric correction of SeaWiFS imagery for turbid coastal and inland waters. *Applied Optics*, 39, 897–912.
- Shi, W., & Wang, M. (2009). An assessment of the black ocean pixel assumption for MODIS SWIR bands. *Remote Sensing of Environment*, 113, 1587–1597.
- Shi, W., & Wang, M. (2014). Ocean reflectance spectra at the red, near-infrared, and short-wave infrared from highly turbid waters: A study in the Bohai Sea, Yellow Sea, and East China Sea. *Limnology and Oceanography*, 59, 427–444.
- Stumpf, R., Arnone, R., Gould, R., Martinolich, P., & Ransibrahmanakul, V. (2003). A partially coupled ocean-atmosphere model for retrieval of water-leaving radiance from SeaWiFS in coastal waters. *NASA Tech Memo 206892* (pp. 51–59).
- Vanhellemont, Q., Bailey, S., Franz, B., & Shea, D. (2014). Atmospheric correction of Landsat-8 imagery using SeaDAS. *ESA Special Publication SP-726. Presented at the 2014 European Space Agency Sentinel-2 for Science Workshop, Frascati*.
- Vanhellemont, Q., Greenwood, N., & Ruddick, K. (2013). Validation of MERIS-derived turbidity and PAR attenuation using autonomous buoy data. *ESA Special Publication SP-722. Presented at the 2013 European Space Agency Living Planet Symposium, Edinburgh*.
- Vanhellemont, Q., Neukermans, G., & Ruddick, K. (2014). Synergy between polar-orbiting and geostationary sensors: Remote sensing of the ocean at high spatial and high temporal resolution. *Remote Sensing of Environment*, 146, 49–62.
- Vanhellemont, Q., & Ruddick, K. (2014a). Turbid wakes associated with offshore wind turbines observed with Landsat 8. *Remote Sensing of Environment*, 145, 105–115.
- Vanhellemont, Q., & Ruddick, K. (2014b). Landsat-8 as a precursor to Sentinel-2: Observations of human impacts in coastal waters. *ESA Special Publication SP-726. Presented at the 2014 European Space Agency Sentinel-2 for Science Workshop, Frascati*.
- Vermote, E., Tanré, D., Deuzé, J., Herman, M., Morcrette, J., & Kotchenova, S. (2006). *Second simulation of a satellite signal in the solar spectrum-vector (6SV)*. 6S User Guide Version 3.
- Wang, M. (2007). Remote sensing of the ocean contributions from ultraviolet to near-infrared using the shortwave infrared bands: Simulations. *Applied Optics*, 46, 1535–1547.
- Wang, M., & Shi, W. (2005). Estimation of ocean contribution at the MODIS near-infrared wavelengths along the east coast of the US: Two case studies. *Geophysical Research Letters*, 32. <http://dx.doi.org/10.1029/2005GL022917> (L13606).
- Wang, M., & Shi, W. (2006). Cloud masking for ocean color data processing in the coastal regions. *IEEE Transactions on Geoscience and Remote Sensing*, 44, 3196–3105.
- Wang, M., & Shi, W. (2007). The NIR-SWIR combined atmospheric correction approach for MODIS ocean color data processing. *Optics Express*, 15, 15722–15733.
- Wang, M., & Shi, W. (2012). Sensor noise effects of the SWIR bands on MODIS-derived ocean color products. *IEEE Transactions on Geoscience and Remote Sensing*, 50, 3280–3292.

- Wang, M., Shi, W., & Jiang, L. (2012). Atmospheric correction using near-infrared bands for satellite ocean color data processing in the turbid western Pacific region. *Optics Express*, 20, 741–753.
- Werdell, P.J., Franz, B.A., & Bailey, S.W. (2010). Evaluation of shortwave infrared atmospheric correction for ocean color remote sensing of Chesapeake Bay. *Remote Sensing of Environment*, 114, 2238–2247.
- Zhu, Z., & Woodcock, C.E. (2012). Object-based cloud and cloud shadow detection in Landsat imagery. *Remote Sensing of Environment*, 118, 83–94.
- Zibordi, G., Holben, B., Slutsker, I., Giles, D., D'Alimonte, D., Mélin, F., et al. (2009). AERONET-OC: A network for the validation of ocean color primary products. *Journal of Atmospheric and Oceanic Technology*, 26.